Spatiotemporal analysis of Portevin–Le Châtelier deformation bands: Theory, simulation, and experiment

P. Hähner,[1,2,*] A. Ziegenbein,[2] E. Rizzi,[3] and H. Neuhäuser[2]
[1]*European Commission, DG-Joint Research Centre, Institute for Energy, PO Box 2, NL-1755 ZG Petten, The Netherlands*
[2]*Technische Universität Braunschweig, Institut für Metallphysik und Nukleare Festkörperphysik, Mendelssohnstr. 3, D-38106 Braunschweig, Germany*
[3]*Politecnico di Bari, Facoltà di Ingegneria di Taranto, Dipartimento di Ingegneria Civile e Ambientale, Via Orabona 4, I-70125 Bari, Italy*

(Received 4 May 2000; revised manuscript received 5 September 2001; published 20 March 2002)

In many solid solutions plastic deformation becomes unstable at sufficiently high temperature due to dynamic strain aging, i.e., repeated breakaway of dislocations from their solute clouds and recapture by mobile solutes, producing stress serrations in constant strain-rate tests or strain bursts in constant stress-rate tests. The instabilities of this well-known Portevin–Le Châtelier (PLC) effect are closely connected with localization of strain in ''PLC deformation bands'' with a width of the order of the specimen thickness and sometimes propagating like a soliton along the specimen. In the present work, the nucleation and propagation of PLC deformation bands is studied by means of a multizone laser scanning extensometer, providing information on local strain along the main part of the specimen, in addition to the conventional measurement of stress serrations. This enables one to differentiate clearly between the bands of types A, B, and C, and to explore their ranges of existence at various temperatures, stresses and strain rates as well as transitions between them along the stress-strain curve. The laser extensometer provides independent data on propagation rate, concentrated strain and width of the bands. These experimental data are compared with a theoretical space-time analysis of propagating PLC bands, which explicitly combines a physical description of the kinetics of dynamic strain aging and plastic deformation. This model provides not only analytical predictions for the above band parameters and their dependences on deformation rate and specimen thickness for Type-A PLC bands, but—by considering types B and C as perturbation modes—is also able to explain the observed transitions between the various types of deformation bands. Moreover, the effect of strain hardening on the appearance of PLC strain localization is elucidated. The analytical predictions are validated by numerical simulations of the model and by comparing them to the experimental findings reported here.

DOI: 10.1103/PhysRevB.65.134109 PACS number(s): 62.20.Fe, 05.45.Yv, 05.65.+b, 81.05.Bx

I. INTRODUCTION

The Portevin–Le Châtelier (PLC) effect, which manifests itself by serrations in the load trace or sudden elongations during plastic deformation of many alloys in a certain range of temperatures, strain rates, and appropriate predeformation, is one of the most prominent examples of plastic instabilities. Discovered in the 19th century by Savart and Masson, and first investigated systematically in the 1920s by Portevin and Le Châtelier, the PLC effect was explained in principle by Cottrell,[1] who proposed the now famous concept of ''dynamic strain aging'' (DSA) by solute diffusion with dislocation breakaway from and recapture in solute ''clouds'' (with an important modification by Sleeswyk[2]). In the period following, this effect was extensively exploited by experiments in the 1970s (e.g., Refs. 3–12), 1980s (e.g., Refs. 13–19), and 1990s (e.g., Refs. 20–27), with increasing refinement of phenomenological modeling (e.g., Refs. 28–42).

While the temperature and strain rate dependences strongly suggest solute diffusion in and around the moving dislocations as the main reason for the PLC effect, contributions from deformation-induced vacancies were discussed[4,11] to explain the observed strain dependence of the PLC range. More important, however, appears the evolution of the dislocation population[29,32,42] and the cooperative interaction between dislocations[40,41], while the suggestion to explain the PLC effect from cooperative dislocation motion without diffusion[43,44] seems restricted to certain conditions (i.e., high local stresses).

The prominent role of solute diffusion in the PLC effect in solid solutions was recently established by detecting three different diffusion mechanisms in Cu-Mn and Cu-Al alloys[21–25,45] which, due to their different stacking-fault energies, permit one to distinguish between solute pipe diffusion in the core region (''lower'' temperatures) and in the stacking fault ribbon between the partial dislocations (''intermediate'' temperatures), while bulk diffusion prevailing at more elevated temperatures finally causes the disappearance of the PLC effect, as the diffusional motion of solutes keeps up with the dislocation motion such that breakaway can no longer occur.[46,47]

While the kinetics of DSA, with its effect on the effective activation energy for dislocation motion, was thoroughly studied in macroscopic stress-strain experiments,[21–25] another important feature of PLC behavior is less well understood, i.e. the development and propagation of localized deformation bands,[31,33,34] which in some cases resemble the Lüders phenomenon. From the appearance of the recorded load serrations, three types of PLC bands have commonly been distinguished:[5,14,17] type-A bands, which are nucleated near one specimen grip during a slight yield point, and then

propagate continuously along the specimen with only slight load fluctuations; type-B bands, which are also nucleated near one grip, but propagate discontinuously along the specimen accompanied by rather regular load serrations; and type-C bands, which nucleate at random along the specimen length and cause strong regular load drops at rather high frequency.

Only few investigations of the band propagation behavior exist, the most thorough one by Chihab *et al.*[18] on Al-Mg alloys and a more general one by Zuev *et al.*,[48] and controversial discussions about the mechanism of propagation and selection of propagation velocity have persisted in the literature for several years (cf. Ref. 34 and references therein). As propagation micromechanisms, either a cross-slip of screw dislocations,[49] dislocation pile-ups at grain boundaries,[50] or intergranular compatibility stresses[33] have been suggested, as well as nonuniaxial stress fields arising from local shear (the Bridgman factor[51]).

In the following we report recent experimental investigations on PLC behavior in Cu-Al polycrystals. By employing a laser scanning extensometer technique, the ranges of existence of the various types of PLC bands, their propagation behavior, and their local strains are investigated systematically in dependence on the temperature, strain rate, grain size, and specimen thickness (Sec. II). Since theoretical results on those PLC band parameters are not available, we formulate a theoretical approach in Sec. III which, by combining in an explicit way (and not only phenomenologically as in previous attempts) the kinetics of dynamic strain aging with that of plastic deformation, provides predictions for the types and propagation rates of PLC deformation bands without resorting to further microstructural assumptions.

Having identified the transition to plastic instability (Hopf bifurcation from a stable focus to a limit cycle behavior) and the range of occurrence of the PLC effect by a linear stability analysis (Sec. IV), we address the problem of PLC band propagation both from theoretical and numerical points of view. Approximate solutions of the nonlinear model describing uniformly propagating solitary waves (type-A bands) are derived in Sec. V. Analytical expressions for the band parameters are presented, which are in good agreement with numerical simulations and the experimental results reported in this work. Furthermore, in Sec. VI, strain-rate regimes where uniform band propagation either becomes unstable with respect to jerky propagation (type B) or tends to be suppressed (type C) are explored, using perturbation theoretical methods. In this way, a qualitative understanding of the various types of PLC bands and their ranges of occurrence, as observed experimentally, is obtained.

II. EXPERIMENT

The fact that the load instabilities associated with the PLC effect are closely related to spatiotemporally inhomogenous plastic deformation is well established.[52] From the experimental point of view, however, a direct observation of strain localization in PLC deformation bands is not straightforward. Usually clip-on extensometers with a limited gauge length are used. Most experiments were performed using one or two clip-on extensometers to approximately determine characteristic deformation band parameters such as the band velocity c_b, the band strain concentration $\Delta\epsilon_b$, and the bandwidth w_b. To the disadvantage of this technique, strains can be observed only in a very limited part of the sample, whereas observation of the whole specimen gauge length is required in order to correlate the PLC events. In an earlier investigation by Chihab *et al.*,[18] this was achieved by a special illumination and video technique, but these observations did not permit the determination of the local plastic strains within the PLC bands.

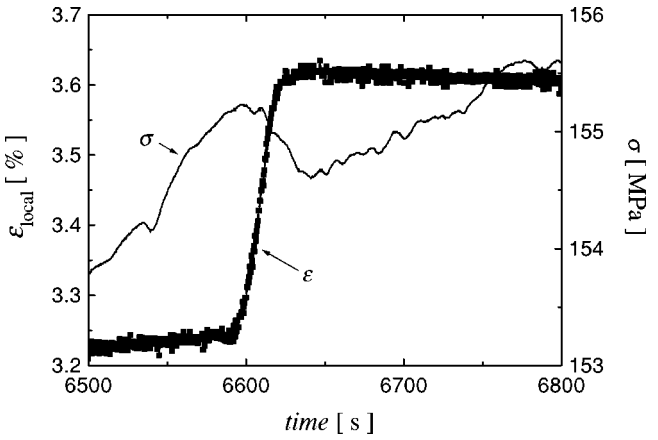

FIG. 1. Increase of the local tensile strain vs time observed within a single specimen zone (zone width 2 mm) and the corresponding stress vs time curve during the passage of a PLC type-A band (Cu-15 at. %Al, $T=323$ K, $\dot{\epsilon}_{,t}=6.67\times10^{-6}$ s^{-1}).

To obtain the relevant parameters describing inhomogeneous deformation in the PLC regime, polycrystalline Cu-15 at. %Al samples (specimen dimensions $75\times4\times1.4$ mm^3, grain sizes $70\ldots530$ μm) were deformed, applying a wide range of strain rates ($6.7\ldots5300\times10^{-6}$ s^{-1}) and deformation temperatures ($273\ldots573$ K). The tensile experiments were performed using a multizone laserscan extensometer. To this end, up to 22 white reflector markings (width 1 mm, spacing 1 mm) are applied on the sample surface, such that each pair, consisting of a white and of an unlacquered segment, represents an extensometer of 2-mm gauge length. The markings are detected from the reflected signal of a laser beam scanned along the specimen axis by means of a prism rotating at a constant frequency (50 Hz). Local strains associated with the displacement of the segment edges are then determined from the time delay between two successive recordings of reflections from the same marking. In this way the laser extensometry allows for a simultaneous recording of the local strains of up to 22 neighboring extensometer zones at a frequency of 50 Hz along a total gauge length of 44 mm. In addition to the high spatiotemporal resolution, this technique offers the advantage of being noncontacting. Contrary to traditional clip-on extensometry, the strain measurement itself can, therefore, not affect the nucleation and propagation of the PLC bands.

As an example for the strain localization associated with the PLC effect, Fig. 1 shows the abrupt increase of the local

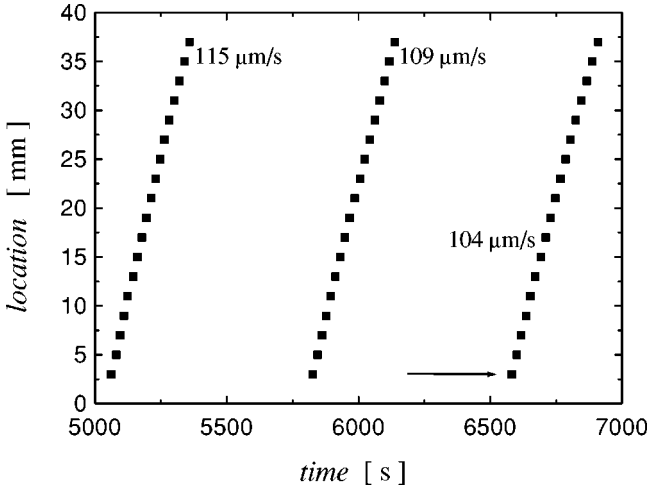

FIG. 2. Correlation diagram showing the location of deformation events vs time, as it is characteristic of the correlated propagation of PLC bands of type A. The propagation velocities of the three successive bands are determined from the slopes. The arrow indicates the event shown in the previous figure.

tensile strain during the passage of a PLC band across one extensometer zone. The corresponding global stress-strain curve reflects the stress drop that goes along with the nucleation of the deformation band. The strain record indicates a localized tensile strain of 0.4% (a local extension of one zone divided by the zone length) carried by the PLC band. An important feature of PLC deformation is the strongly correlated propagation and repeated nucleation of successive PLC bands. To reveal this correlation, the location (extensometer zone) of any abrupt strain increase caused by the passage of a PLC band is plotted versus its time of occurrence. Figure 2 is an example of such a correlation plot, where the propagation of three successive PLC bands is clearly visible. This orderly propagation of a solitary deformation band is denoted as PLC type A according to the above-mentioned classification of PLC types.[5,14,17,52,53]

During deformation at temperatures $T<425$ K, a transition from PLC type A to type C has been observed. This type is characterized by rapid serrations in the stress-strain curve with each stress drop indicating a sharp local increase in strain (Fig. 3). As opposed to type A, these strain bursts do not spread as solitary waves along the specimen axis, but they appear at random positions along the gauge length without propagation (Fig. 4). Hence the spatiotemporal correlation of plastic deformation is much less pronounced in this case. (Strictly speaking, these type-C bands are not completely uncorrelated but tend to self-avoid, since each band is associated with some local strain hardening.) The transition from type A to type C with increasing strain is accompanied by a decrease in the local strain concentration. This is an indication of a decreasing efficiency of DSA which, ultimately, leads to the disappearance of the PLC effect at even larger strains due to an exhaustion effect.[25] More commonly, the transition from type A to type C can be observed by decreasing the applied strain rate or increasing the deformation temperature (Figs. 7 and 8 below).

PLC bands of type B were observed only in the higher

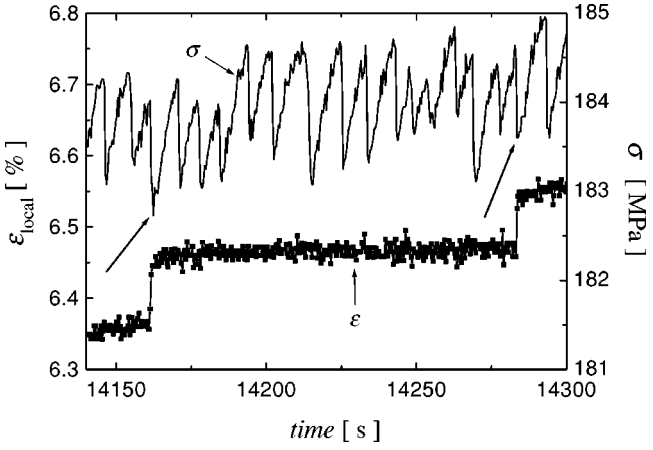

FIG. 3. Two successive strain bursts in a single specimen zone and the recorded stress drops vs time characterizing PLC type C; the marked stress drops correspond to the two local deformation events ($T=383$ K, $\dot{\epsilon}_{,t}=6.67\times10^{-6}$ s^{-1}).

range of temperatures $T>425$ K. Similar to the PLC type C, each stress drop is accommpanied by a strain burst, now localized in the front of the advancing deformation band (Fig. 5). In contrast to PLC type C, the strain bursts are strongly correlated as they relate to a discontinuous (stop-and-go) propagation of the band (Fig. 6).

According to Nortmann and Schwink,[23] who investigated the diffusion processes responsible for DSA in Cu-10 at. %Al, the activation enthalpy for solute diffusion can be determined from the transitions between the various PLC types and stable deformation behavior. If one plots the reduced stress at which the PLC type changes as a function of temperature and strain rate, the critical stresses limiting the PLC regimes show an Arrhenius-type behavior in terms of $1/T$ (Fig. 7) and $\log\dot{\epsilon}$ (Fig. 8). Assuming that the boundaries of the PLC regimes represent the deformation states at which the plastic strain rate matches the aging rate by solute diffusion, the activation energy for the diffusion process control-

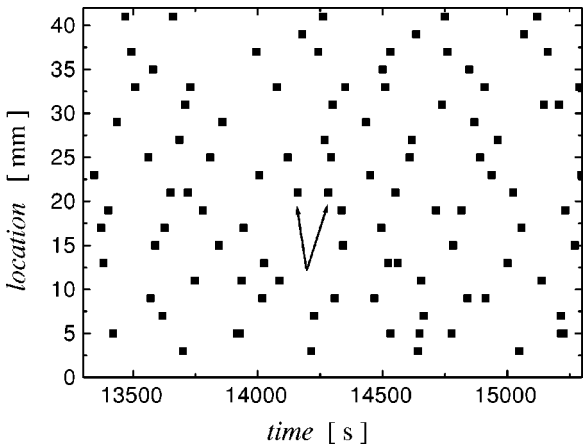

FIG. 4. Correlation diagram of deformation events characterizing the uncorrelated PLC type C. While the two arrows indicate the strain bursts shown in the previous figure, other events are noted in the time slot in between.

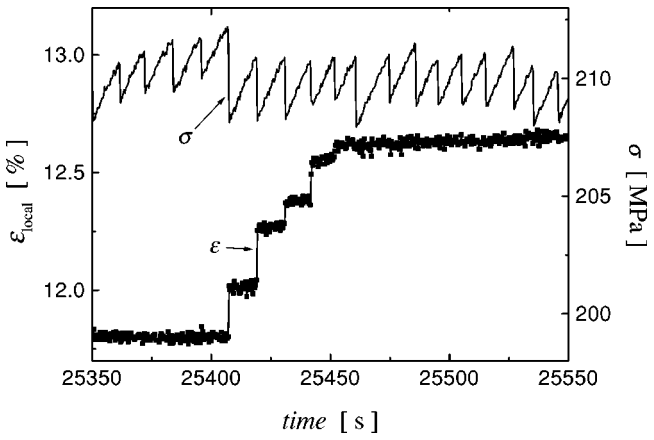

FIG. 5. Stepwise increase of the local tensile strain vs time in a single specimen zone and the corresponding stress drops vs time during the discontinuous passage of a type-B band ($T=473$ K, $\epsilon_{,t}=6.67\times10^{-6}$ s^{-1}).

ling DSA follows directly from the slopes of the Arrhenius plots. For the present Cu-15%Al alloy the activation energy is $Q=0.74\pm0.05$ eV, which, within the limits of confidence, agrees with the value determined for an α-phase CuAl-alloy.[23,54] This activation energy is less than half the volume diffusion energy $Q_D\approx2$ eV. The ratio $Q/Q_D\approx0.4$ is typical of a pipe-diffusion process along the dislocation cores, as estimated by Balluffi and Granato[55]: $Q_{\rm pipe}/Q_D \approx 0.3\ldots0.7$.

An important point for the understanding of PLC band dynamics is the effect of various material parameters, such as grain size, and of the specimen geometry on the band velocity c_b, the bandwidth w_b, the local tensile strain rate $\epsilon_{b,t}$, and the tensile strain increment $\Delta\epsilon_b$ concentrated in the band. Provided that the band propagates uniformly, those characteristic band parameters are related to the applied crosshead velocity v according to $v=\Delta\epsilon_b c_b$ and $v=\epsilon_{b,t}w_b$. The first relation expresses the solitary wave character of a type-A deformation band (the strain-rate profile preserves its shape during propagation), whereas the second relation states that the whole applied strain rate is accommodated inside a narrow band of width w_b (the deformation activity outside the band is negligible).

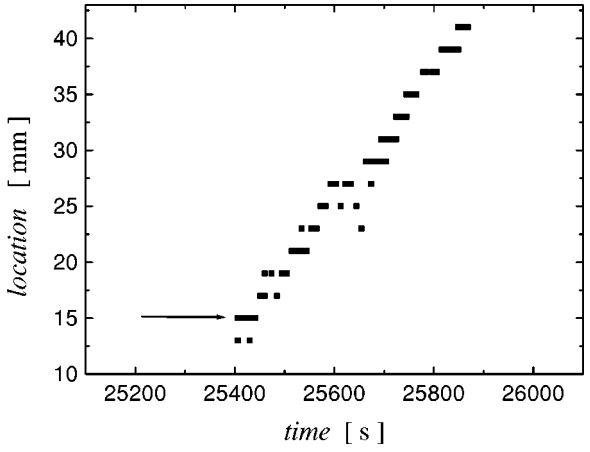

FIG. 6. Correlation diagram of deformation events characterizing the discontinous propagation of a PLC band of type B. The arrow indicates the series of strain bursts shown in the previous figure.

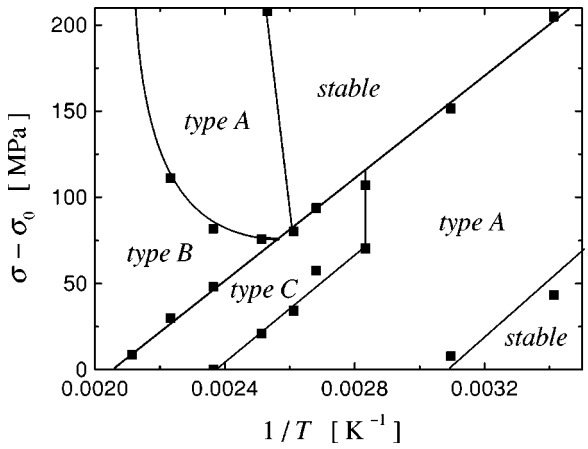

FIG. 7. Map of the regimes of different PLC types for Cu-15 at. %Al, as characterized by the reduced tensile stress $\sigma-\sigma_0$ and reciprocal temperature ($\epsilon_{,t}=6.67\times10^{-6}$ s^{-1}).

In earlier investigations usually only one of the parameters: grain size, temperature, or strain rate was varied. As laser extensometry allows the simultaneous observation of all band parameters by a single measurement, more extensive parameter studies have become possible. Here we report on systematic observations of band parameters for various temperatures, strain rates, grain sizes, and sample thicknesses. As the strain rate is increased systematically by about three orders of magnitude, the band strain, the bandwidth and the band velocity are observed to increase (Fig. 9). It is important to note that all of these parameters have been determined independently without making use of the solitary wave properties. As one infers from the double-logarithmic plots, the strain-rate dependences are well fitted by power laws with the exponents given in the inset of Fig. 9. One notes that the band velocity c_b is not directly proportional to the applied strain rate, because the band strain $\Delta\epsilon_b$ also increases

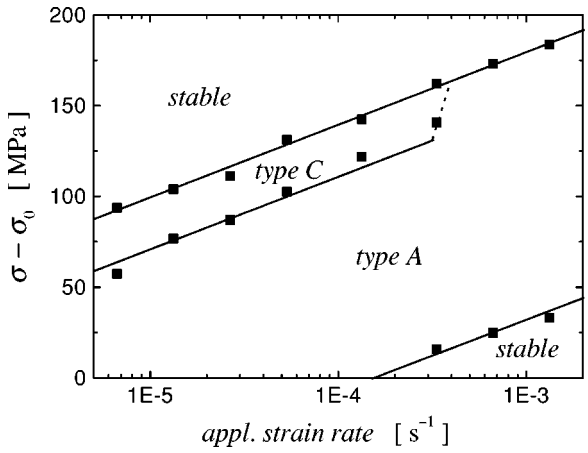

FIG. 8. Map of the regimes of different PLC types, as characterized by the reduced tensile stress $\sigma-\sigma_0$ and the logarithmic applied strain rate ($T=373$ K).

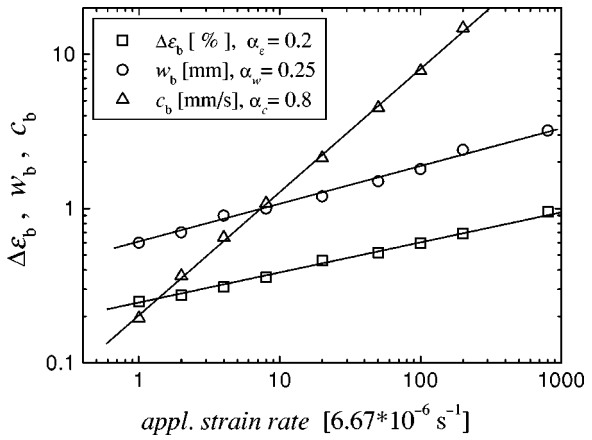

FIG. 9. Double-logarithmic plots of the band strain $\Delta\epsilon_b$, the bandwidth w_b, and the band velocity c_b as functions of applied strain rate at $T=373$ K.

slightly with increasing strain rate. While this trend had been noted before,[56] the present work confirms this behavior more accurately for a wider range of strain rates. According to $v=\Delta\epsilon_b c_b$, the exponents of $\Delta\epsilon_b$ and c_b should add to unity. The fact that this is the case confirms the solitary character of the type-A deformation bands. While the bandwidth w_b shows a similar trend as the band strain $\Delta\epsilon_b$,[56,57] the present observations indicate that the corresponding exponents are slightly different: 0.25 and 0.2, respectively. Results by Chihab *et al.*[18] who reported w_b to decrease with increasing strain rate in an Al alloy, seem to be at variance with the present observations. However, it should be noted that those measurements refer to PLC type B. At higher deformation temperatures (423 . . . 573 K), where Cu-15%Al exhibits a type B band, we also observed the inverse behavior of $w_b(v)$.[58]

From experimental[3,59,60] as well as theoretical points of view,[33,41,61] there is an interest in the effect of the grain size d on the PLC band dynamics. It was proposed that intergranular compatibility stresses provide the spatial coupling between adjacent volume elements that controls the propagation of the PLC bands.[61] To clarify the question as to the

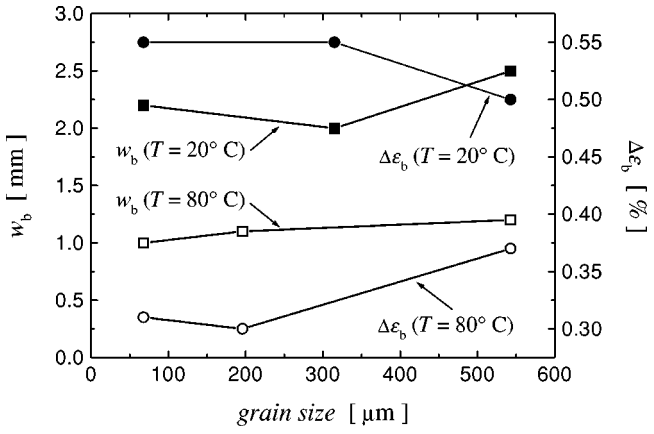

FIG. 10. Variation of the band strain $\Delta\epsilon_b$ and the bandwidth w_b in dependence on the grain size d at 293 and 353 K for Cu-15 at. %Al (full symbols: $T=293$ K; open symbols: $T=353$ K).

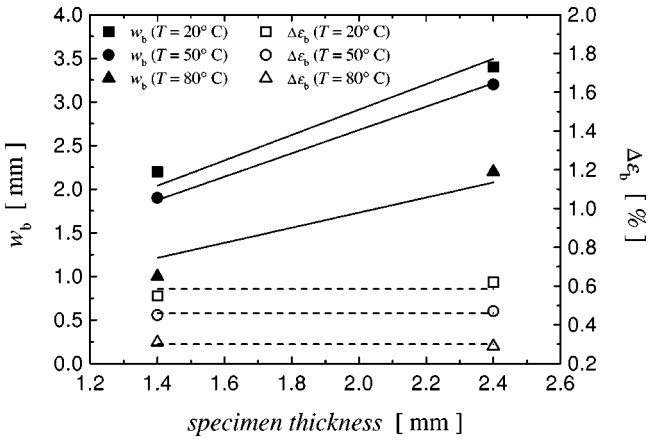

FIG. 11. Dependence of the band strain $\Delta\epsilon_b$ and the bandwidth w_b on the specimen thickness s, as determined for three different deformation temperatures (full symbols: w_b, open symbols: $\Delta\epsilon_b$). The solid lines are linear regressions through the origin, and the dashed lines are horizontal linear regressions.

relevant propagation mechanism, tensile tests were performed for three different grain sizes in the range 70 μm $\leqslant d \leqslant$ 530 μm. The results show almost no grain size effect on the PLC band strain $\Delta\epsilon_b$ and the bandwidth w_b (Fig. 10). According to the solitary wave properties, this also implies that the band velocity c_b is unaffected by d, which has been confirmed by independent measurements. This compares with early results on α-brass reported by Munz and Macherauch,[3] provided that the proper reduced-stress intervals are considered. (Some grain-size dependence can be noted as to the onset of the PLC effect. For instance, at $T=293$ K type-A fluctuations set in at 4.7% strain for a grain size of 70 μm, whereas deformation is stable until 9.1% strain for the coarse grain size of 530 μm. Hence results should not be compared at constant strain, but at constant reduced stress, in order to describe the d dependence of the PLC band parameters. From this point of view, results reported for an Al-Mg-Si alloy in Ref. 59 also show no significant effect of d on the PLC dynamics.) The absence of grain size effects on the band parameters, especially on the band width, suggests that intergranular compatibility stresses are not controlling PLC band propagation.

As opposed to grain size, the specimen thickness s does possess an important influence on the appearance of PLC bands.[57] To see this, we conducted a series of tests with s increased from 1.4 to 2.4 mm. From Fig. 11 one gathers that the bandwidth w_b increases in proportion to s, while the band velocity c_b and the band strain $\Delta\epsilon_b$ are almost unaffected. This is in accordance with observations on an Al-Mg-Si-alloy.[57]

The identification of the prevailing propagation mechanism and its implementation in a spatiotemporal PLC model have to be done in the light of these results. Before we come back to this point in Sec. V, we are going to present a new model of the PLC effect (Sec. III), and discuss some of its basic properties (Sec. IV).

III. FORMULATION OF THE MODEL

A major objective of the present work is to formulate a PLC model which goes beyond previous models, inasmuch

as DSA is to be considered on a physical base. This is a prerequisiste for a quantitative interpretation of the experimental findings. At the same time, the model should be kept simple enough as to allow for the derivation of analytical solutions for the fundamental properties of plastic deformation bands (band velocity, width, and strain) and for the conditions of occurrence of the various band types (A, B, and C). To combine these goals let us start from the previous idea[9] that aging occurs while glide dislocations are temporarily arrested at localized barriers (e.g., forest dislocations) that are overcome by means of thermal activation. This is expressed by an Arrhenius law for the plastic strain rate $\epsilon_{,t}$ with an effective Gibbs' free activation enthalpy $G=G_0+\Delta G$:

$$\epsilon_{,t}=\nu\Omega\exp\left[-\frac{G_0+\Delta G}{kT}+\frac{\sigma_{\rm eff}}{S_0}\right]. \tag{1}$$

Here ν is an appropriate attack frequency, Ω is the elementary strain accomplished when all mobile dislocations have been activated once, G_0 is the basic activation enthalpy in the absence of DSA, k is the Boltzmann constant, and T is the absolute temperature. The additional, DSA-related enthalpy ΔG represents an internal variable of our model. Since ΔG is in proportion to the solute content accumulated at the glide dislocations, the plastic strain rate $\epsilon_{,t}$ depends on the aging history.

Thermal activation is facilitated by the effective stress which drives the mobile dislocations,

$$\sigma_{\rm eff}(\epsilon,\epsilon_{,t},\Delta G)=\sigma_{\rm ext}(\epsilon,\epsilon_{,t},\Delta G)-\sigma_{\rm int}(\epsilon), \tag{2}$$

and which is defined as the externally applied stress $\sigma_{\rm ext}$ (flow stress) diminished by the internal stress $\sigma_{\rm int}$ (athermal back stress). Owing to strain hardening, the latter depends explicitly on the plastic strain ϵ. Finally, the *instantaneous* strain-rate sensitivity (SRS) of the flow stress is denoted by $S_0=\partial\sigma_{\rm ext}/\partial\ln\epsilon_{,t}|_{\epsilon,\Delta G}$. This quantity describes the material's response in the absence of variations in strain hardening *and* aging state, i.e., processes which cannot respond instantaneously to changes in strain rate.

According to the premise that aging occurs during the waiting time of mobile dislocations at obstacles, ΔG increases with increasing waiting time and, hence, decreasing strain rate. While this has been recognized to be the origin of strain-rate softening instability, here we do without *a priori* fixing the strain-rate dependence of ΔG, but consider this quantity as a dynamical internal variable of the model which is allowed to depend not only on the momentary value of $\epsilon_{,t}$, but also on the strain-rate history. This idea is closely related to distinguishing the instantaneous SRS S_0 which is always positive, from the *asymptotic* SRS S_∞,

$$S_\infty=\left.\frac{\partial\sigma_{\rm ext}}{\partial\ln\epsilon_{,t}}\right|_\epsilon=S_0+\left.\frac{\partial\sigma_{\rm ext}}{\partial\Delta G}\right|_\epsilon\frac{d\Delta G}{d\ln\epsilon_{,t}}, \tag{3}$$

which accounts for the material's response observed after the internal degrees of freedom associated with DSA have relaxed to a new steady state. S_∞ describes the effect of DSA under stationary deformation conditions. Plastic instability then goes along with negative values of S_∞ (strain-rate softening instability).

In principle, the temporal evolution of ΔG can be obtained from solving the solute drift-diffusion problem in the stress field of a dislocation. While this is a formidable task in itself, that has been solved formally for special cases only (cf. Ref. 62), we note that the ΔG dynamics incorporates two counteracting effects: (i) strain aging itself gives rise to an increase of ΔG with time, while (ii) unpinning of dislocations is accompanied by the loss of the solute cloud such that ΔG is reset to zero. DSA then encompasses the combination of these effects, which is taken into account by the following differential equation:

$$\partial_t\Delta G=\eta\left(\frac{\Delta G_\infty}{\Delta G}\right)^{(1-n)/n}(\Delta G_\infty-\Delta G)-\frac{\epsilon_{,t}}{\Omega}\Delta G. \tag{4}$$

Here n denotes the characteristic exponent of the aging kinetics (see below) and η is the aging rate which is in proportion to the solute mobility. One notes that, even in the case $n=1$ (linear aging), Eq. (4) is strongly nonlinear owing to the ΔG dependence of $\epsilon_{,t}$ [cf. Eq. (1)] which figures in the depinning term.

The role of the aging term [first term on the right-hand side of Eq. (4)] is clarified if one considers *static* aging ($\epsilon_{,t}=0$). Then one has $\partial_t\Delta G=\eta(\Delta G_\infty/\Delta G)^{(1-n)/n}(\Delta G_\infty-\Delta G)$, which reproduces the well-known behavior as a function of aging time (waiting time): (i) For small waiting times, $t\ll\eta^{-1}$ and $\Delta G\ll\Delta G_\infty$, the initial behavior is governed by $\partial_t\Delta G=\eta\Delta G_\infty^{1/n}\Delta G^{1-1/n}$. Integrating with the initial condition $\Delta G(0)=0$ then gives the power law $\Delta G\approx\Delta G_\infty(\eta t/n)^n$ with the aging exponent n. As a matter of fact, n depends on the specific type of dislocation pinning by solute atoms (lineal pinning along the dislocation line, or pointlike pinning at the intersections of the dislocation with forest dislocations[63]), and on the mode of solute diffusion (bulk diffusion or pipe diffusion along forest dislocations[63]). [Many experimental investigations point at $n=1/3$ (Refs. 21–25) which is associated to DSA by pipe diffusion of solute atoms along the dislocation lines.] (ii) For long waiting times, $t\gg\eta^{-1}$ and $\Delta G\approx\Delta G_\infty$, one has $\partial_t\Delta G=\eta(\Delta G_\infty-\Delta G)$, meaning that aging saturates exponentially according to $\Delta G\approx\Delta G_\infty(1-\exp[-\eta t])$. Hence ΔG_∞ is seen to represent the ''aging potential'' given by the maximum increase of the activation enthalpy experienced by completely aged dislocations.

The second term on the right-hand side of Eq. (4) stands for the decay of ΔG due to the thermally activated depinning of dislocations. As during depinning the solute cloud around the glide dislocation is released, the solute content (as represented by ΔG) relaxes at the rate $\epsilon_{,t}/\Omega$. One notes that the ΔG dynamics incorporates two characteristic time scales $\Omega/\epsilon_{,t}$ and η^{-1}, a proper balance of which represents a necessary condition for strain-rate softening instability to occur. This will be elaborated in more detail in Sec. IV.

As the plastic strain rate [Eq. (1)] depends not only on the aging state ΔG but is also controlled by the effective stress $\sigma_{\rm eff}$ at which the system is operating, the model equation (4)

has to be coupled to the mechanical behavior of the system. Instead of $\sigma_{\rm eff}$ itself, it is more convenient to consider the generalized driving force

$$f \equiv \frac{\nu}{\eta}\exp\left[-\frac{G_0}{kT}\right]\exp\left[\frac{\sigma_{\rm eff}}{S_0}\right] \tag{5}$$

as a nondimensional control variable. The temporal evolution of f decomposes into a contribution from the externally applied stress rate $\sigma_{{\rm ext},t}$ and a contribution from the rate of increase of the internal stress due to strain hardening [cf. Eq. (2)]: $\partial_t f=(\sigma_{{\rm ext},t}/S_0-h\epsilon_{,t}/S_0)f$. Here we have assumed a linear strainhardening, $\sigma_{\rm int}=h\epsilon$, where $h=\partial\sigma_{\rm ext}/\partial\epsilon|_{\epsilon_{,t},\Delta G}$ denotes the strain-hardening coefficient. This assumption does not represent any loss of generality for the subsequent analysis, as the plastic strain carried by a deformation band is sufficiently small as to ensure quasilinear hardening with parametric changes in h only.

Using definition (1) of the plastic strain rate, $\epsilon_{,t}=\eta\Omega\exp[-\Delta G/(kT)]f$, we finally arrive at the following set of constitutive equations:

$$\partial_t f=\frac{\sigma_{{\rm ext},t}}{S_0}f-\frac{\eta\Omega h}{S_0}\exp\left[-\frac{\Delta G}{kT}\right]f^2, \tag{6}$$

$$\partial_t \Delta G=\eta\left(\frac{\Delta G_\infty}{\Delta G}\right)^{(1-n)/n}(\Delta G_\infty-\Delta G)-\eta f\exp\left[-\frac{\Delta G}{kT}\right]\Delta G. \tag{7}$$

Unless constant stress-rate testing ($\sigma_{{\rm ext},t}=$const) is considered, this has to be supplemented with the machine equation for a tensile test,

$$\sigma_{{\rm ext},t}=E_{\rm eff}\left(\frac{v}{l}-\frac{1}{l}\int_0^l dx\,\eta\Omega\exp\left[-\frac{\Delta G}{kT}\right]f\right), \tag{8}$$

according to which the elastic strain rate and the overall plastic strain rate combine to comply with the imposed crosshead velocity v. Here we have introduced the gauge length l of the tensile specimen and the effective elastic modulus $E_{\rm eff}$ of the tensile system composed of the specimen and the machine.

IV. BASIC PROPERTIES OF THE MODEL

Equations (6)–(8) represent the nonlinear coupling between the aging kinetics [Eq. (7)] and the mechanical behavior of the tensile system [Eqs. (6) and (8)]. Before investigating the model, it is convenient to introduce scaled variables to reduce the number of independent parameters. In

$$\dot f=\dot\sigma f-\theta\exp[-g]f^2, \tag{9}$$

$$\dot g=(g/g_\infty)^{-m}(g_\infty-g)-f\exp[-g]g, \tag{10}$$

$g=\Delta G/(kT)$ and $g_\infty=\Delta G_\infty/(kT)$ denote the nondimensional additional free enthalpy and its value at saturation, respectively, and a dot stands for differentiation with respect to non-dimensional time $\tilde t=\eta t$. The exponent m is defined as $m=(1-n)/n$. Moreover, we have introduced dimensionless parameters by scaling the stress rate and the strain hardening coefficient according to $\dot\sigma=\sigma_{{\rm ext},t}/(\eta S_0)$ and $\theta=\Omega h/S_0$, respectively.

In what follows we consider *linear aging*, with $n=1$ and $m=0$, for simplicity. [Although this ''standard model'' seems not to have a physical realization, it already exhibits all the salient features of a strain-rate softening instability, and it shares the behavior of the deformation band parameters with the general case $m>0$ (cf. Sec. V). A generalization of the results to non-standard aging is straightforward, but detracts from the compactness of representation.] In this case, Eq. (10) reduces to

$$\dot g=g_\infty-g-f\exp[-g]g. \tag{11}$$

To investigate the possibility of strain-rate softening instability associated with Eqs. (9) and (11), one calculates the asymptotic SRS as defined by Eq. (3):

$$S_\infty=S_0\left(1-\frac{g_\infty}{[1+\epsilon_{,t}/(\eta\Omega)]^2}\frac{\epsilon_{,t}}{\eta\Omega}\right). \tag{12}$$

We note that DSA provides a negative SRS contribution which may outbalance S_0 and, hence, gives rise to $S_\infty<0$ provided that the aging potential is sufficiently large ($g_\infty>4$) and that the plastic strain rate matches the aging rate ($\epsilon_{,t}\approx\eta\Omega$).

Additional information about the loss of stability is obtained from linear stability analysis of Eqs. (9) and (11). If one introduces $(\delta f,\delta g)=(f-f_{\rm s},g-g_{\rm s})$ as the deviations of f and g from the steady-state values

$$f_{\rm s}=\frac{\dot\sigma}{\theta}\exp\left[\frac{g_\infty}{1+\dot\sigma/\theta}\right],\quad g_{\rm s}=\frac{g_\infty}{1+\dot\sigma/\theta} \tag{13}$$

and linearizes with respect to δf and δg, one obtains

$$\begin{pmatrix}\dot{\delta f}\\ \dot{\delta g}\end{pmatrix}=\begin{pmatrix}-\dot\sigma & \dot\sigma f_{\rm s}\\ -\dfrac{\dot\sigma}{\theta}\dfrac{g_{\rm s}}{f_{\rm s}} & \dfrac{\dot\sigma}{\theta}(g_{\rm s}-1)-1\end{pmatrix}\begin{pmatrix}\delta f\\ \delta g\end{pmatrix}. \tag{14}$$

With $(\delta f,\delta g)=(\delta f_0,\delta g_0)\exp[\lambda t]$ one calculates the eigenvalues λ of the evolution matrix,

$$\lambda_\pm=\kappa\pm\sqrt{\kappa^2-\omega^2}, \tag{15}$$

with

$$\kappa=\frac{1}{2}\left(\frac{\dot\sigma}{\theta}(g_{\rm s}-1-\theta)-1\right),\quad \omega^2=\dot\sigma\left(\frac{\dot\sigma}{\theta}+1\right). \tag{16}$$

The requirement that the real part of λ become positive as instability sets in is tantamount to the condition $\kappa>0$, or $\dot\sigma/\theta>1/(g_{\rm s}-1-\theta)$. Using definition (13) of $g_{\rm s}$ yields

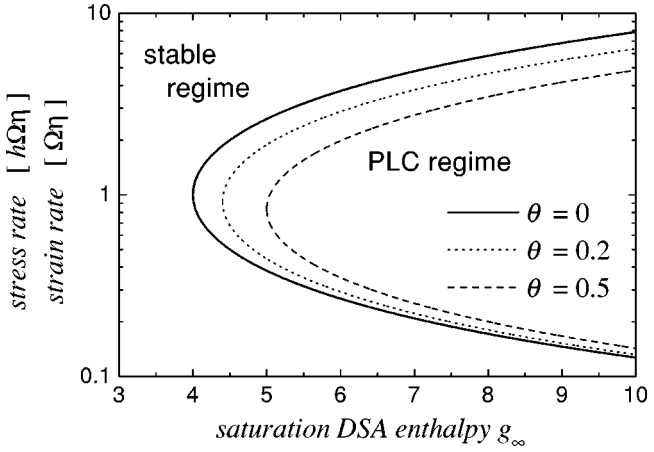

FIG. 12. Semilogarithmic plot of the unstable stress-rate range [PLC regime as defined by Eq. (17)] as a function of $g_\infty = \Delta G_\infty / kT$ for various dimensionless strain hardening rates θ. Note that the stress rates map to strain rates according to $\epsilon_{,t} = \sigma_{\mathrm{ext},t}/h$.

$$\frac{[g_\infty - 2 - \theta - \sqrt{g_\infty(g_\infty - 4 - 2\theta)}]}{2(1+\theta)} < \frac{\dot\sigma}{\theta} < \frac{[g_\infty - 2 - \theta + \sqrt{g_\infty(g_\infty - 4 - 2\theta)}]}{2(1+\theta)} \tag{17}$$

for the unstable range of stress rates. The corresponding strain-rate range follows immediately from the equivalence $\epsilon_{,t} = \eta\Omega\dot\sigma/\theta$ under steady-state deformation conditions. Figure 12 shows the PLC range in a semilogarithmic plot. One notes that the PLC range shrinks as the hardening rate is increased, meaning that strain hardening has a stabilizing effect. In the absence of strain hardening ($\theta = 0$), $g_\infty > 4$ is a necessary condition for instability to occur.

The condition $\kappa = 0$ defines the onset of an oscillatory instability associated with a *Hopf bifurcation* from a stable focus to an unstable one: $\lambda(\kappa = 0) = \pm i\omega$. [The Hopf bifurcation is subcritical meaning that the unstable range (as predicted by linear stability analysis) is surrounded by a metastable range where instability can be triggered by the presence of (finite-amplitude) noise.[64] In practice, the transition to deformation localization is facilitated by intrinsic strain-rate fluctuations induced by dislocation interactions and by quenched-in fluctuations of the material parameters.] This represents a generic feature of velocity-softening instabilities associated with solid friction and earthquake dynamics[65] or thermomechanical instabilities at low-temperature plastic deformation.[41] The unstable focus is surrounded by a limit cycle in the phase plane (f,g). In a spatially extended system (*viz.* the gauge length of the tensile specimen), the revolution around this limit cycle corresponds to the repeated nucleation and propagation of deformation bands (Sec. V).

Figure 13 gives an example of a limit cycle which was calculated numerically and plotted together with the zeros of Eqs. (9) and (11):

$$\dot f = 0 \quad \Rightarrow \quad f_{\mathrm{s}}^{(f)} = \frac{\dot\sigma}{\theta}\exp g \tag{18}$$

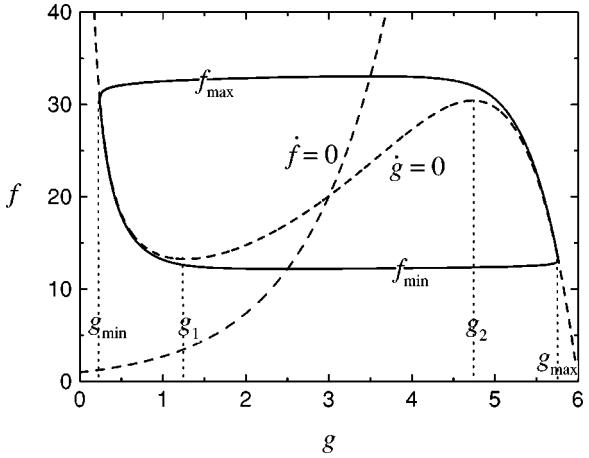

FIG. 13. Limit cycle (solid line) in the (f,g) plane as calculated numerically for a weak hardening case ($\dot\sigma = \theta = 10^{-2}$, $g_\infty = 6$). The intersection of the characteristic curves $\dot f = 0$ and $\dot g = 0$ (dashed lines) defines the unstable working point of the system. In the weak hardening case, the values of $f_{\mathrm{max,min}}$ and $g_{\mathrm{min,max}}$ are approximately fixed by the extrema of the $\dot g = 0$ characteristic (adiabatic approximation) at $g_{1,2}$, respectively.

and

$$\dot g = 0 \quad \Rightarrow \quad f_{\mathrm{s}}^{(g)} = \left(\frac{g_\infty}{g} - 1\right)\exp g. \tag{19}$$

The parameters $\dot\sigma = \theta = 0.01$ and $g_\infty = 6$ were chosen such that the steady state ''working point'' (intersection point $\dot f = \dot g = 0$) lies on the unstable ascending branch of the $\dot g = 0$ characteristic. For sufficiently small values of θ, the mechanical behavior of the system as represented by Eq. (9) is slow as compared to the aging kinetics in g [Eq. (11)]. As Fig. 13 illustrates for $\theta = 0.01$, the nonmonotonic behavior of the $\dot g = 0$ characteristic then causes a bistable switching of the system in the (f,g) phase plane. Most of the time the system stays close to the stable descending branches of $\dot g = 0$ (tantamount to an adiabatic approximation with respect to the fast variable g which follows the slow evolution of f). Close to the extrema of the $\dot g = 0$ characteristic, however, the system has to switch from one stable branch to the other one, as the unstable ascending branch is inaccessible. The switching occurs on a fast time scale such that f is almost unable to follow ($f \approx$ const), which is why the actual contour of the limit cycle is governed by the $\dot g = 0$ characteristic.

Figure 14 shows another limit cycle calculated for faster hardening: $\dot\sigma = \theta = 0.5$, $g_\infty = 6$. In this case, time scales are not separable, and the four intersection points of the limit cycle and the characteristic curves $\dot f = 0$ and $\dot g = 0$ just define the horizontal and the vertical tangents of the limit cycle, respectively, while the system no longer evolves close to $\dot g = 0$. A quantitative distinction between the cases of weak and strong hardening is postponed to Sec. V.

In concluding this section, we point to the close analogy which exists between the present problem (isothermal plastic

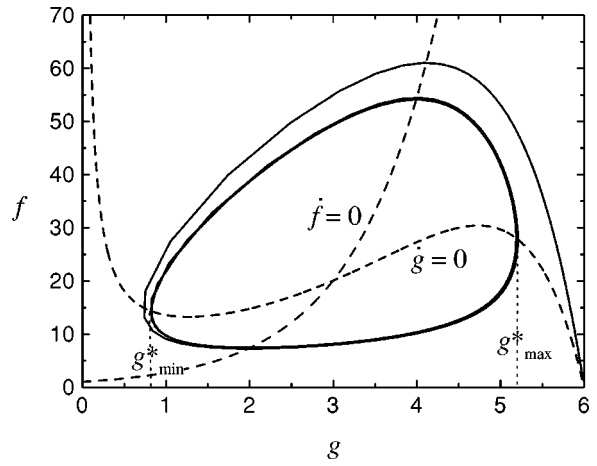

FIG. 14. Example of a numerically calculated limit cycle (solid line) pertaining to strong hardening [$\dot{\sigma}=\theta=0.5$, $g_\infty=6$; initial condition: $g(0)=6$, $f(0)=10^{-3}$]. The characteristic curves (dashed lines) coincide with those shown in Fig. 13. Note that g cannot fall below θ, while the adiabatic approximation for g is no longer valid anywhere.

deformation in the presence of DSA) and thermomechanical instabilities during low-temperature plastic deformation (plasticity coupled to deformation-induced generation of heat).[41] Returning to the Arrhenius law [Eq. (1)], one notes that the internal variable ΔG of the DSA problem plays much the same role as (reciprocal) temperature T in the thermomechanical problem. As illustrated in Table I, the evolution equation (4) then compares to the energy balance: depinning acts like a heat source due to the dissipation of mechanical work, and strain aging corresponds to heat losses to the surrounding bath. In both cases, instability is due to a positive feedback between the internal variable and the plastic strain rate. In view of this formal analogy it is not surprising that the phenomenological aspects of thermomechanical deformation at low temperatures closely resemble the PLC effect (localized deformation bands, serrated stress-strain curves). In fact, also in thermomechanics an instantaneous SRS (response to adiabatic changes in strain rate) and an asymptotic SRS (temperature T relaxed to dynamical equilibrium) have to be distinguished, and bands of types A and C can be discerned.[41] While in the thermomechanical problem, heat conduction provides a diffusionlike spatial coupling, it is not obvious which coupling mechanism prevails in the PLC problem. This question is addressed in Sec. V.

TABLE I. Comparison between the Portevin–Le Châtelier effect and thermomechanical instabilities.

PLC effect	Thermomechanical problem
$\epsilon_{,t}=\nu\Omega\exp\left[-\frac{G_0}{kT}-g+\frac{\sigma_{\rm eff}}{S_0}\right]$	$\epsilon_{,t}=\nu\Omega\exp\left[-\frac{G_0}{kT}+\frac{\sigma_{\rm eff}}{S_0}\right]$
$\dot{g}=g''-(g-g_\infty)-(\epsilon_{,t}/\eta\Omega)g$	$\dot{T}=T''-(T-T_0)+\epsilon_{,t}\sigma_{\rm ext}$
spatial coupling ?	heat conduction
strain aging	heat losses to bath
depinning	dissipation of mechanical work
$g\searrow \rightleftharpoons \epsilon_{,t}\nearrow$	$T\nearrow \rightleftharpoons \epsilon_{,t}\nearrow$

V. CALCULATION OF TYPE-A DEFORMATION BAND PARAMETERS

A. Band propagation and effect of strain hardening

In order to relate plastic instability to the concomitant strain localization in deformation bands, some kind of spatial coupling has to be introduced, as was suggested in earlier work by Aifantis.[66] Formally this coupling provides a propagation mechanism for the deformation bands, as a characteristic length scale is introduced, which affects the width of the bands. While, for symmetry reasons, the leading-order coupling is expected to be a second-order gradient term with respect to the tensile x coordinate, the physical nature of the prevailing propagation mechanism remains a controversial issue.[61] In principle, band propagation may be provided either by some *extrinsic* mechanism (related to specimen geometry and deformation conditions) or be an *intrinsic* material property.

In Appendix A, where various propagation mechanisms are discussed, we argue for long-range dislocation interactions governing the band propagation in rate-insensitive materials. As mobile dislocations correlate over a distance $\xi \propto S_\infty^{-1/2}$,[67–69] loss of strain-rate sensitivity ($S_\infty\to 0$ corresponds to an infinite stress sensitivity) goes along with a diverging dislocation correlation length. Macroscopic dislocation correlations associated with the PLC effect were confirmed by glide band observations[46] and acoustic emission techniques.[70] In the context of the present work it is interesting to note that the observed influence of the specimen thickness can then be attributed to a finite-size effect, as ξ cannot exceed the transversal specimen dimension. In Appendix A we estimate the dislocation correlations to result in a diffusionlike coupling in the dynamics of g with the pseudodiffusion coefficient $D_g\approx\beta_g g_{\min}(\mu/S_0)\epsilon_{b,t}s^2$. Here μ is the shear modulus, and $\beta_g\approx 0.1$ a geometry factor which combines details pertaining to the dislocation arrangement and to the inclination of the deformation bands with respect to the tensile axis (cf. Appendix A). Inserting typical experimental parameter values, D_g is estimated to be of the order of 1 mm^2/s. Hence the spatial coupling provided by dislocation correlations is sufficient to explain the observed band widths from a quantitative point of view (Sec. V C).

In the following we investigate the deformation banding associated with the second-order gradient introduced in the dynamics of g,

$$\dot{f}=\dot{\sigma}f-\theta\exp[-g]f^2, \tag{20}$$

$$\dot{g}=g''+g_\infty-g-f\exp[-g]g, \tag{21}$$

where primes stand for differentiation with respect to the dimensionless spatial coordinate $\tilde{x}=\sqrt{\eta/D_g}x$. Let us focus on deformation bands of type A which, once nucleated, are solitary waves that propagate along the tensile axis at a constant speed such that the band strain $\Delta\epsilon_b$ accommodates vir-

tually the whole applied strain rate v/l. Then the relationships $v=\Delta\epsilon_b c_b$ and $v=\epsilon_{b,t} w_b$ hold between the propagation speed c_b, the local plastic strain rate in the band $\epsilon_{b,t}$, and the bandwidth w_b. While it is readily verified that such a particular solution type exists for Eqs. (20) and (21), the stability issue of the solitary wave solution is postponed to Sec. VI.

To calculate the band parameters, we note that solitary waves fulfill $\dot{f}=-cf'$ and $\dot{g}=-cg'$ with $c=(D_g\eta)^{-1/2}c_b$, denoting the nondimensional band speed, and that the dimensionless stress rate $\dot{\sigma}$ can be neglected to a good approximation during band propagation. [The $\dot{\sigma}$ term in Eq. (20) is only appreciable during the quasielastic deformation preceding the nucleation of a new band, whereas during the propagation of a fully developed band the effect of strain hardening in the band largely exceeds that of the applied stress rate.] Then Eqs. (20) and (21) read

$$cf'-\theta\exp[-g]f^2=0, \tag{22}$$

$$g''+cg'-f\exp[-g]g+g_\infty-g=0. \tag{23}$$

Before we analyze this set of nonlinear ordinary differential equations, we have to consider in more detail the effect of the strain hardening coefficient θ on the limit cycle behavior displayed by Figs. 13 and 14.

According to the definition of the plastic strain rate, $\epsilon_{,t}=\eta\Omega f\exp[-g]$, the peak strain rate in a deformation band corresponds to a relative maximum of $f\exp[-g]$ or $g'=f'/f$. Combining this with Eqs. (22) and (23), for the band strain rate one finds

$$\frac{\epsilon_{b,t}}{\eta\Omega}=\frac{g_\infty-g^*_{\min}+g''}{g^*_{\min}-\theta}, \tag{24}$$

where $g^*_{\min}$ denotes the residual DSA enthalpy which is actually realized at the peak strain rate (cf. Fig. 14). As $g^*_{\min}$ cannot fall below θ (singularity), deviations from the switching-curve approximation must become appreciable as θ approaches $g_{\min}$ from below. This is evident from a comparison of the limit cycles shown in Figs. 13 and 14, respectively. To determine the critical value at which finite-hardening effects become appreciable, we compare θ with the minimum value of the DSA enthalpy, $g_{\min}$, in the switching-curve approximation (Fig. 13). For $g_\infty\gg 1$ one readily calculates $g_{\min}$ from Eqs. (18) and (19): $g_{\min}\approx g_\infty(g_\infty-1)\exp[-(g_\infty-1)]$, which amounts to about 0.2 for $g_\infty=6$ and becomes as small as 2×10^{-6} for $g_\infty=20$. Accordingly, the transition from weak to strong hardening occurs for

$$\theta=\frac{h\Omega}{S_0}\geqslant g_\infty(g_\infty-1)\exp[-(g_\infty-1)]. \tag{25}$$

Owing to this exponential g_∞ dependence, weak hardening (and, hence, the validity of the switching-curve approximation) is realized only if DSA is not too strong, say $4<g_\infty<8$. In the following subsections we derive analytical approximations of the band parameters for weak hardening and strong hardening, and compare the results with numerical simulations and with the experimental findings reported in Sec. II, respectively.

B. Weak hardening regime

1. Analytical results

To proceed with the calculation of the band velocity c, Eq. (23) is multiplied by g' and integrated along the tensile axis. This yields

$$c=\frac{\int_{-\infty}^{+\infty}d\tilde{x}fgg'\exp[-g]}{\int_{-\infty}^{+\infty}d\tilde{x}(g')^2}=\frac{I_1}{I_2}. \tag{26}$$

After integration by parts and inserting Eq. (22), the numerator I_1 reads

$$I_1=\frac{\theta}{c}\int_{-\infty}^{+\infty}d\tilde{x}(1+g)(f\exp[-g])^2. \tag{27}$$

This integral can be evaluated if one notes that $\epsilon_{,t}=\eta\Omega f\exp[-g]$ is a sharply localized function that can be approximated by a δ function. For weak hardening ($\theta\ll g_{\min}$), we obtain

$$I_1=\frac{\theta}{c}(1+g_{\min})\left(\frac{\epsilon_{b,t}}{\eta\Omega}\right)^2 w \tag{28}$$

where $w=\sqrt{\eta/D_g}\,w_b$ is the dimensionless band width.

For the evaluation of the denominator I_2 in the regime of weak hardening, one notes that, according to the switching-curve approximation, the deformation band profile is divided into three substages $w=w_{\rm I}+w_{\rm II}+w_{\rm III}$, with different approximations pertaining to different types of dynamics. As illustrated schematically by Fig. 15, stages I and III correspond to the rapid depinning of dislocations in the front and to the rapid recapturing in the wake of the band, respectively. These stages are associated with the switching of g at virtually constant values $f=f_{\max}$ and $f=f_{\min}$, respectively, which follow from the extrema of the $\dot{g}=0$ characteristic (Fig. 13). In the intermediate stage II, however, g is in equilibrium with the evolution of f (adiabatic approximation $\dot{g}=0$) and, hence, the dynamics is controlled by strain hardening [Eq. (22)]. As g' is negligible in stage II, the denominator of Eq. (26) is approximated by

$$I_2=(g_{\max}-g_{\min})^2\left(\frac{1}{w_{\rm I}}+\frac{1}{w_{\rm III}}\right)\approx 2(g_{\max}-g_{\min})^2. \tag{29}$$

Here it should be noted that unity width of substages I and III is assumed, $w_{\rm I}\approx w_{\rm III}\approx 1$, which represents just a rough order of magnitude estimate. Again $g_{\max}$ and $g_{\min}$ are defined by the extrema of $\dot{g}=0$ (Fig. 13).

To estimate the width $w_{\rm II}$ of the central part of the band, we use Eq. (23) in the adiabatic approximation, $g'\approx g''\approx 0$, according to which $f\exp[-g]\approx g_\infty/g-1\approx g_\infty/g_{\min}-1$. Inte-

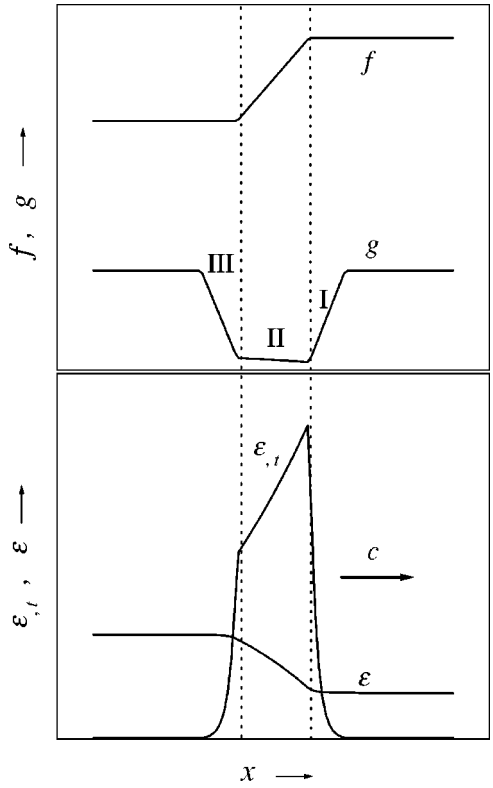

FIG. 15. Schematic illustration of a solitary deformation band in terms of f and g (upper part), as well as $\epsilon_{,t}$ and ϵ (lower part). A clear distinction between the three substages (I: unpinning; II: rapid glide; III: recapturing) can be made in the weak hardening regime only, while for strong hardening the profiles are smeared out.

gration of Eq. (22) yields $c\ln(f_{\max}/f_{\min})=\theta(g_\infty/g_{\min}-1)w_{\rm II}$, and according to definition (5), one has $\ln f_{\max}/f_{\min}=\theta\Delta\epsilon_b/\Omega$, and therefore

$$w_{\rm II}=\frac{g_{\min}}{g_\infty-g_{\min}}\frac{v}{\Omega\sqrt{D_g\eta}}. \tag{30}$$

Note that the actual value of the strain-hardening coefficient has dropped from this expression.

Combining Eqs. (28)–(30) and returning to dimensional units, we obtain the following set of band parameters in the *weak hardening regime*:

$$c_b=\left(\frac{D_g}{\eta}\right)^{1/4}\frac{\sqrt{(1+g_{\min})/2}}{g_{\max}-g_{\min}}\sqrt{\theta}\,\frac{v}{\Omega\sqrt{w_b}}, \tag{31}$$

$$w_b=2\sqrt{\frac{D_g}{\eta}}+\frac{g_{\min}}{g_\infty-g_{\min}}\frac{v}{\eta\Omega}, \tag{32}$$

$$\Delta\epsilon_b=\frac{v}{c_b}. \tag{33}$$

We note that the functional dependencies of c_b, w_b, and $\Delta\epsilon_b$ on the crosshead velocity v remain valid for any aging kinetics with $n\neq 1$. While systematic simulations of the present PLC model will be presented elsewhere,[71] some exemplary numerical results are discussed in the following subsection, proving the validity of results (31)–(33).

2. Numerical simulations

In order to check the accuracy of Eqs. (31)–(33), numerical integrations of Eqs. (20) and (21) and the machine equation (8) have been performed in the weak hardening regime. The model parameters assumed for the simulation are the following: $\eta=0.1\ \mathrm{s}^{-1}$, $\Omega=10^{-5}$, $S_0=1$ MPa, $E_{\rm material}=E_{\rm machine}=10^5$ MPa ($E_{\rm eff}=0.5\times10^5$ MPa), $f(0)=10^{-13}$, $g(0)=g_\infty=6$, $D_g=10^{-7}\ \mathrm{m}^2/\mathrm{s}$, and $l=0.1$ m. The governing equations are discretized both in time and in space, and solved through a fully implicit finite-difference integration scheme on the space coordinate at each time step. A nondimensional time step $\Delta\tilde{t}=0.1$ and an array of 100 segments (''blocks'') along the specimen length have been considered. Fixed boundary conditions have been imposed, namely, for the first and last blocks, $\dot{f}=\dot{g}=0$ at each instant of time. To trigger the PLC instability, the initial condition $f(0)$ is perturbed in space by a random multiplicative factor varying between 1 and 30, which alters the local yield strength by up to 10%.

Figure 16 (top) shows numerical results concerning type-A PLC band propagation for an applied strain rate of $v=1\times10^{-7}$ m/s, right in the center of the PLC range. In this case, PLC band nucleation is triggered by an initial perturbation at the second block only. Parabolic plastic strain hardening is prescribed by a nondimensional hardening coefficient which decreases parametrically with the spatially averaged plastic strain $\epsilon_{\rm av}$ according to the linear dependence $\theta=\theta_0-2\times10^{-6}(\epsilon_{\rm av}/\Omega)$, where $\theta_0=\Omega h_0/S_0=10^{-2}$ is the initial nondimensional hardening coefficient corresponding to $h_0=10^3$ MPa. During the imposed loading history, the resulting hardening parameter h then ranges from 1000 to about 200 MPa. Note that the corresponding nondimensional hardening coefficient is $\theta=0.01\ldots0.002$, such that $\theta\ll g_{\min}\approx0.6$ refers to the weak hardening case. In Fig. 16 (top) the space-time correlation map of the strain-rate activity is displayed together with the post-yield stress evolution in time. The correlation map is derived from the full plastic strain rate field by scoring a mark in the space-time plane whenever the local plastic strain rate reaches a relative maximum above a certain threshold. The information about the band propagation behavior obtained in this way, can be compared to the space-time correlation plots from laser extensometry (Sec. II). The PLC bands are seen to propagate smoothly through the specimen and display a reflective pattern of type A. The corresponding stress-time curve shows a staircase profile, which is typical of this zig zag propagation mode.[58]

As another example, Fig. 16 (bottom) summarizes the numerical simulation of a tensile test with the same parabolic hardening, but at somewhat lower crosshead velocity, namely, $v=0.6\times10^{-7}$ m/s. Here the initial conditions for f are perturbed by a random factor at all blocks. Again the space-time correlation map is shown together with the corresponding stress-time curve. A full spectrum of PLC bands ranging from type C to A is observed during the tensile test,

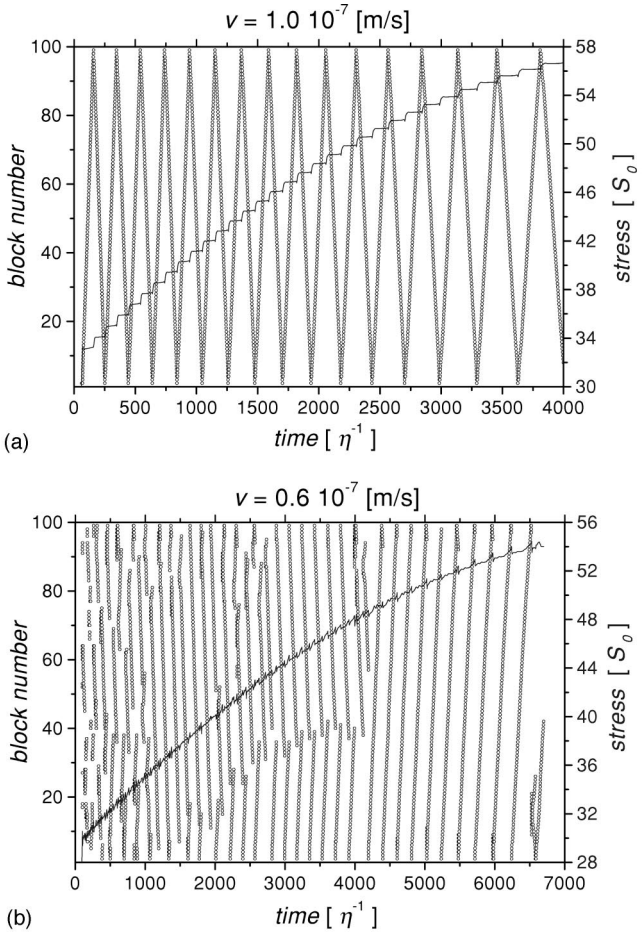

FIG. 16. Uniaxial tensile tests simulated under constant applied crosshead velocity $v=1.0\times10^{-7}$ m/s (top) and $v=0.6\times10^{-7}$ m/s (bottom), with the parameters $\eta=0.1$ s^{-1} and $S_0=1$ MPa in both cases: space-time correlation map of strain-rate activity (left axis, scatter plot with circles) and post-yield stress-time curve (right axis, continuous line).

in qualitative agreement with experimental observations. Initially, isolated plastic strain bursts of type C erupt randomly along the specimen length. Then, as the hardening coefficient θ decreases, the plastic bursts tend to correlate in time and space to form PLC bands partially traveling and hopping through the specimen. Genuine type-B propagation sets in toward the second half of the loading history. Later on, at even lower θ, these bands stabilize further and approach the fully correlated type-A propagation mode. As opposed to the previous case, the type-A bands now repeatedly propagate in the same direction, giving rise to a serrated stress-time curve.[58]

Those patterns have been observed in the whole PLC range, depending on the simulated strain rate and the hardening rate. As a general trend, it has been noted that types-C and -B bands are favored during the initial loading phase (large hardening rate) and towards the lower bound of the strain rate range where the PLC instability develops, whereas a type-A band prevails at high strain rate and-or low hardening rate. A theoretical interpretation of these observations will be given in Sec. VI.

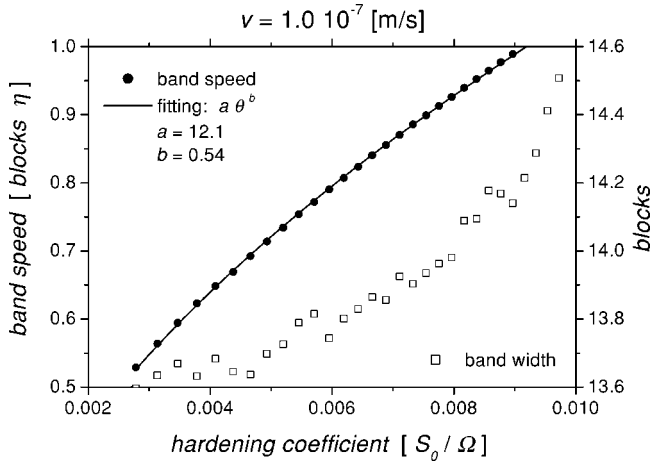

FIG. 17. Numerical results of a uniaxial tension test simulated at constant applied crosshead velocity $v=1.0\times10^{-7}$ m/s ($\eta=0.1$ s^{-1}, $S_0=1$ MPa, $\Omega=10^{-5}$). Band speed (left axis, numerical results represented by solid symbols, power-law fit by full line) and band width (right axis, open symbols) vs hardening coefficient.

The type-A band velocity c_b and bandwidth w_b for $v=1\times10^{-7}$ m/s are represented in Fig. 17 as a function of the imposed hardening coefficient θ. The band velocity is calculated from the slopes of the space-time correlation patterns shown in Fig. 16 (top), while the bandwidth is determined from the base width at threshold of the plastic strain rate bursts. One notes that w_b is virtually independent of θ in accordance with Eq. (32), noting some minor variation owing to the strain-hardening dependence of the variable $g_{\min}$. The variation range of w_b in Fig 17 is actually confined to one block, i.e., 1/100 of the specimen length. Quantitative accordance with Eq. (32) is achieved for $2\sqrt{D_g/\eta}=2$ blocks and $g_{\min}\approx0.6$.

It is apparent from Figs. 16 (top) and 17 that c_b decreases, while θ is decreasing during the tensile test, in good agreement with the square root dependence predicted by Eq. (31); see the power law fit $c_b\propto\theta^{0.54}$ shown in Fig. 17. The band velocities range from about 0.05 to 0.10 blocks per second, which, with the assumed length $l=0.1$ m divided into 100 blocks, translates into 0.05–0.10 mm/s. With $g_{\min}=0.6$ the simulated band velocities are about twice as large as the theoretical results [Eqs. (31) and (32)]. This discrepancy represents an immediate consequence of the crude approximation made in the last step of Eq. (29). In fact, better agreement results if the factor of 2 is suppressed there.

In order to check the functional dependence of the band velocity c_b on the bandwidth w_b predicted by Eq. (31), it is convenient to plot $c_b\sqrt{w_b/\theta}$ as a function of the imposed strain rate v/l for various simulation runs performed with different constant hardening coefficients in the weak hardening range, $10^{-3}\leqslant\theta\leqslant10^{-2}$, and with linearly increasing strain rates. Figure 18 confirms that the data almost collapse on a common straight line through the origin, as expected from Eq. (31), and proving the validity of analytical expressions (31) and (32). Moreover, we have checked that Eq. (33) holds, provided that there is not more than one band propagating at any time.

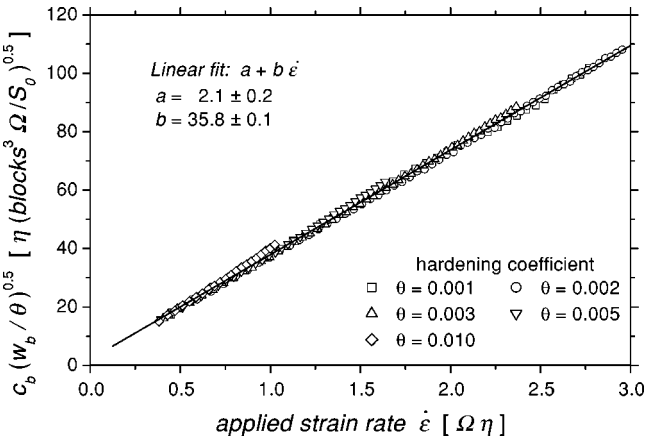

FIG. 18. Numerical results for the rescaled band velocities $c_b\sqrt{w_b/\theta}$ as a function of the applied strain rate $\dot{\epsilon}=v/l$ for various nondimensional hardening coefficients $\theta=(\Omega/S_0)h$ in the weak hardening regime ($\eta=0.1\ \mathrm{s}^{-1}$, $S_0=1$ MPa, $\Omega=10^{-5}$). Note that the data collapse on a common master curve, which is approximately represented by a straight line through the origin. Simulated results (scatter plots) and linear regression fit to all data (full line).

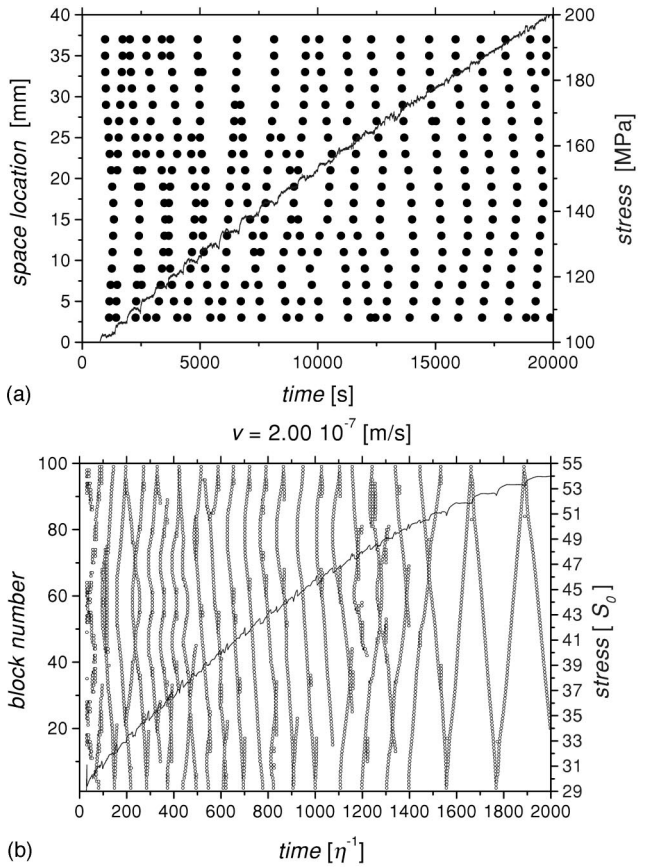

FIG. 19. Comparison between an experimentally observed space-time correlation map of strain-rate activity with the corresponding stress-time curve superimposed (top) and a qualitatively similar numerical simulation result (bottom). Top: polycrystalline Cu-15 at. %Al alloy tested with an applied strain rate of $6.67\times10^{-6}\ \mathrm{s}^{-1}$ at 20 °C (Ref. 58). Bottom: same as Fig. 16, but with $v=2.0\times10^{-7}$ m/s. In both cases, one notes a wealth of PLC band propagation modes, including parallel propagation, zigzag propagation, and multiple band propagation with phase shifts during band collision.

In concluding this subsection, we point at the complexity of band propagation patterns observed experimentally, as well as in the simulations of the model. Figure 19 shows two typical examples of space-time correlation maps of the strain-rate activity, the simulation result (bottom) obtained toward the upper strain-rate range of the PLC regime, the laser extensometric result (top) referring to the lower temperature range of the PLC regime. (Note that for the thermally activated processes under consideration, lowering the temperature has qualitatively the same effect as increasing the strain rate.) In both cases, one observes a variety of band propagation modes: (i) subsequent PLC bands traveling in the same direction (no reflection), (ii) zigzag propagation with reflections at the ends of the specimen, (iii) and multiple band propagation with phase shifts suffered during the collision of bands traveling in opposite directions. While the actual material system certainly exhibits a considerable degree of quenched-in randomness (e.g., flow stress variations due to the polycrystalline structure), it is interesting to see that the present PLC model reproduces those patterns without any element of randomness [except for the random perturbations imposed on the initial condition $f(0)$]. Additional results of systematic numerical simulations of the model are given in Ref. 71.

C. Strong hardening regime

It is obvious from Fig. 14 that the three band substages I–III can no longer be distinguished in the strong hardening regime ($\theta\gtrsim g_{\min}$). To calculate the band parameters, the nondimensional bandwidth w is now identified with the characteristic decay length of f. According to Eq. (22) one has $f'/f=\theta\epsilon_{b,t}/(c\,\eta\Omega)\approx 2/w$ and, hence, $w_b=2\Omega/(\epsilon_{b,t}\theta)c_b$. On the other hand, one easily checks that Eqs. (28) and (29) and, consequently, Eq. (31), continue to hold if $g_{\min}$ and $g_{\max}$ are replaced by the actual extrema $g^*_{\min}$ and $g^*_{\max}$ as introduced in Fig. 14. Combining those equations and using the localization condition $\epsilon_{b,t}w_b=v$, we arrive at the band parameters for the *strong hardening regime*:

$$c_b=\frac{\theta}{2\Omega}v, \tag{34}$$

$$w_b=\frac{2}{\theta}\frac{1+g^*_{\min}}{(g^*_{\max}-g^*_{\min})^2}\sqrt{\frac{D_g}{\eta}}, \tag{35}$$

$$\Delta\epsilon_b=\frac{v}{c_b}=\frac{2\Omega}{\theta}. \tag{36}$$

Again these results approximately hold for any aging kinetics $n\neq 1$, apart from insignificant correction factors of the order of unity. As opposed to the weak hardening case presented above, band velocity and strain do not depend on the spatial coupling provided by the pseudodiffusion coefficient. With $D_g\propto s^2$, this compares to the observation that those

band parameters are not affected by variations in specimen thickness s, whereas the bandwidth scales as $w_b \propto s$.

To compare those results with the experimental findings reported in Sec. II, we note that for Cu-15%Al one has $S_0 \approx 1$ MPa, $\Omega \approx 5\times10^{-4}$, $g^*_{\max} \approx g_\infty \approx 8$, $\eta^{-1} \approx 60$ s, $h \approx 1000$ MPa, and $\mu \approx 4\times10^4$ MPa at $T=353$ K. Hence, $\theta \approx 0.5 \gg g_{\min} \approx 0.05$ such that the strong hardening case is applicable. With a band strain rate $\epsilon_{b,t} \approx 3\times10^{-4}$ s^{-1} observed at the basic applied strain rate $v/l = 6.67\times10^{-6}$ s^{-1}, the pseudodiffusion coefficient (Appendix A) follows as $D_g \approx 1.2$ mm^2 s^{-1}. This leads to the following theoretical band parameters $c_{b,\mathrm{th}} = 0.25$ mm/s, $w_{b,\mathrm{th}} = 0.9$ mm and $\Delta\epsilon_{b,\mathrm{th}} = 0.2$ % which is to be compared with the experimental results from Fig. 9, $c_{b,\mathrm{ex}} = 0.195 \pm 0.01$ mm/s, $w_{b,\mathrm{ex}} = 0.6 \pm 0.2$ mm, and $\Delta\epsilon_{b,\mathrm{ex}} = 0.25 \pm 0.05$%, determined for $v/l = 6.67\times10^{-6}$ s^{-1}. Consequently, quantitative agreement is satisfactory.

Regarding the functional dependence of the band parameters on the applied strain rate, we note that the pseudodiffusion coefficient itself is rate dependent: $D_g \propto \epsilon_{b,t} = v/w_b$. Therefore, the theoretical band parameters obey the power laws $c_{b,\mathrm{th}} \propto v^{\alpha_c}$, $w_{b,\mathrm{th}} \propto v^{\alpha_w}$, and $\Delta\epsilon_{b,\mathrm{th}} \propto v^{\alpha_\epsilon}$ with the exponents $\alpha_c = 1$, $\alpha_w = 1/3$, and $\alpha_\epsilon = 1 - \alpha_c = 0$. The experimental investigations compiled in Fig. 9 yield $\alpha_c = 0.8$, $\alpha_w = 0.25$, and $\alpha_\epsilon = 0.2$, respectively. While the fundamental trends are correct, we note some systematic deviation, inasmuch as the observed band velocities do not completely accommodate the applied strain rate: $\alpha_c < 1$ and $\alpha_\epsilon > 0$. The reason for this discrepancy is related to the fact that material parameters have been assumed to be constant, but actually are not completely rate independent. In particular, this is true for the strain-hardening coefficient h. In fact, if one corrects for the experimentally observed rate dependence of h, the band velocity exponent increases to $\alpha_c = 0.9$, which comes close to the theoretical prediction $\alpha_c = 1$. At present, it cannot be excluded that additional rate corrections have to applied, for instance, to the instantaneous strain-rate sensitivity S_0. Further experiments are required to clarify this point.

VI. ANALYSIS OF BAND TYPES B AND C

From the experimental observations we know that, as the applied strain rate is lowered, the solitary behavior of type-A deformation bands tends to give way to a less regular behavior associated with bands of type B (intermittent propagation) and type C (propagation suppressed). This leads us to investigate the stability of type-A bands with respect to small perturbations. As we shall see, transitions to types B and C can then be related to bifurcations from stable to unstable behavior of type-A bands subjected to certain perturbation modes.

The perturbation analysis, details of which are presented in Appendix B, is performed in the comoving coordinate frame of a type-A band (velocity c) where the band profile is stationary. The analysis applies both to weak and strong hardening. Denoting deviations from stationarity in DSA activation enthalpy g by $\psi(\tilde{x},\tilde{t})$, we arrive at the following linearized equation governing the growth of perturbations of the form $\exp[i\omega\tilde{t}]\psi(\tilde{x})$ with complex-valued frequency $\omega = \Re(\omega) + i\Im(\omega)$:

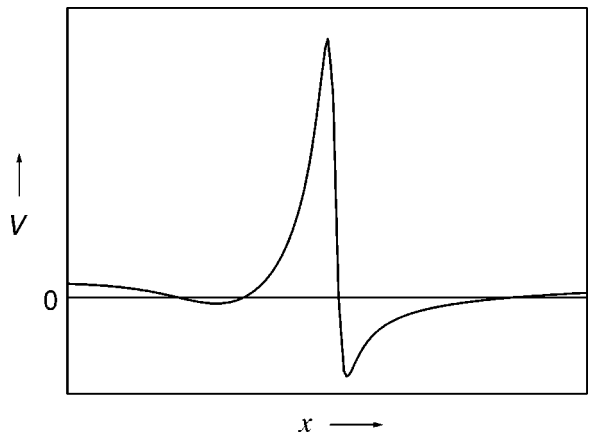

FIG. 20. Plot of the double-well potential [Eq. (B10)] corresponding to the limit cycle shown in Fig. 14. If perturbations which tend to localize in the front (right well) start growing monotonically, a transition from type A to C occurs, whereas oscillating perturbations give rise to a periodically modulated band propagation associated with type B.

$$i\omega\psi + \mathcal{H}\psi = -\mathcal{Y}. \tag{37}$$

The left-hand side of this equation is formally equivalent to a Schrödinger equation with the "Hamiltonian" $\mathcal{H} = -\partial_{\tilde{x}}^2 + \mathcal{V}$, while the right-hand side $\mathcal{Y}$ describes the effect of the feedback of the tensile machine on the aging kinetics [cf. Eq. (B11) of Appendix B]. The "potential" $\mathcal{V}$ which is defined in terms of the unperturbed type-A solution [cf. Eq. (B10)] has the form of a double well. The example depicted in Fig. 20 refers to strong hardening associated with the limit cycle of Fig. 14. Accordingly, perturbations tend to be localized mainly in the front (the deep minimum in $\mathcal{V}(x)$ to the right) and, to a lesser extent, in the wake (the shallow minimum to the left) of the band. In the case of a temporally oscillating and growing perturbation $[\Re(\omega) \neq 0,\ \Im(\omega) < 0]$ this gives rise to a "breathing" of the deformation band which is associated to the discontinuous band propagation of type B in the laboratory coordinate frame. On the other hand, type-C behavior is associated with exponentially growing perturbations without oscillations $[\Re(\omega) = 0,\ \Im(\omega) < 0]$.

To a first approximation (cf. Appendix B) the real and imaginary parts of ω are given by

$$[s_2 - |\lambda_1| - 2\Im(\omega)]\Re(\omega) = 0, \tag{38}$$

$$[\Im(\omega)]^2 - (s_2 - |\lambda_1|)\Im(\omega) + s_1 Y_{11} - s_2|\lambda_1| - [\Re(\omega)]^2 = 0, \tag{39}$$

where $s_1 = [\Omega E_{\mathrm{eff}}/(S_0 l)]\sqrt{D_g/\eta}$ and $s_2 = (E_{\mathrm{eff}} v)/(S_0 \eta l)$ are combinations of material parameters, and Y_{11} is a matrix element defined in Eq. (B15). The ground state of $\mathcal{H}$ with the eigenvalue $\lambda_1 < 0$ represents the only bound state of the eigenvalue problem. From Eqs. (38) and (39), the following conclusions are derived.

(1) For $\Re(\omega) \neq 0$ the solutions to Eqs. (38) and (39) read

$$\Im(\omega)=\frac{s_2-|\lambda_1|}{2},$$

$$\Re(\omega)=\pm\sqrt{s_1Y_{11}-\left(\frac{s_2+|\lambda_1|}{2}\right)^2}. \tag{40}$$

Hence, oscillatory type-B instability is expected to occur for

$$s_2<|\lambda_1|<2\sqrt{s_1Y_{11}}-s_2, \tag{41}$$

where the lower boundary ensures the growth of the perturbation $[\Im(\omega)<0]$ and, hence, the instability of the type-A solution, while the upper bound follows from the requirement that $\Re(\omega)$ be real (oscillatory instability).

(2) For $\Re(\omega)=0$ (no oscillations), Eq. (38) is trivially fulfilled, while Eq. (39) yields

$$\Im(\omega)=\frac{s_2-|\lambda_1|}{2}\pm\sqrt{\left(\frac{s_2+|\lambda_1|}{2}\right)^2-s_1Y_{11}}. \tag{42}$$

The occurrence of a type-C instability then requires

$$|\lambda_1|>2\sqrt{s_1Y_{11}}-s_2. \tag{43}$$

(3) If $s_2>2\sqrt{s_1Y_{11}}-s_2$, namely $s_2>(s_1/s_2)Y_{11}$, the type-B range [Eq. (41)] does not exist, and a type-C instability occurs for

$$|\lambda_1|>\frac{s_1}{s_2}Y_{11}. \tag{44}$$

In principle, inequalities (41)–(44) can be used to set up PLC maps like Figs. 7 and 8 representing the experimental results. However, this necessitates a detailed knowledge of the stress, strain rate, and temperature dependences of the parameters s_1, s_2, Y_{11}, and λ_1. Since a comprehensive discussion of the implications of conditions (41)–(44) is quite intricate, we shall concentrate on the leading dependences on crosshead velocity v, which governs the occurrence of the various band types. To this end it suffices to note that, according to Eqs. (B6) and (B15), one has $s_1=\text{const}(v)$, $s_2\propto v$, and $Y_{11}\propto v^2$. Hence the characteristic functions $(s_1/s_2)Y_{11}$ and $2\sqrt{s_1Y_{11}}-s_2$ both increase in proportion to v, while the modulus of the ground-state eigenvalue $|\lambda_1|$ is a monotonically decreasing function of v [cf. Eqs. (31) and (B10)]. Figure 21 gives a schematic view of those v dependences together with the resulting types of deformation bands. In the upper part of the figure $s_2<(s_1/s_2)Y_{11}$ gives rise to the occurrence of an intermediate type-B regime which is missing in the opposite case $[s_2>(s_1/s_2)Y_{11}$ (lower part)]. Out of the various parameters affecting the ocurrence of type B, we just point out that this oscillating deformation mode is facilitated by a soft machine [the condition $s_2<(s_1/s_2)Y_{11}$ is the easier to fulfill the smaller E_{eff}; cf. Eq. (B6)]. It is important to note that regimes of types A and C may also be absent if their velocity ranges are masked by stable deformation behavior [(cf. result (17) of the linear stability analysis].

The influence of the strain-hardening coefficient θ on the deformation banding is governed by the θ dependence of $|\lambda_1|$ (since s_1 and s_2 are independent of, and Y_{11} depends only weakly on θ). As θ decreases during plastic deformation, $|\lambda_1|$ also decreases, and a type-C behavior tends to give way to a type-A behavior [cf. Eq. (44)]. This trend has been confirmed by the numerical simulations of the model equations (20) and (21), as reported in Sec. V B 2, Fig. 16 (bottom), and Ref. 71.

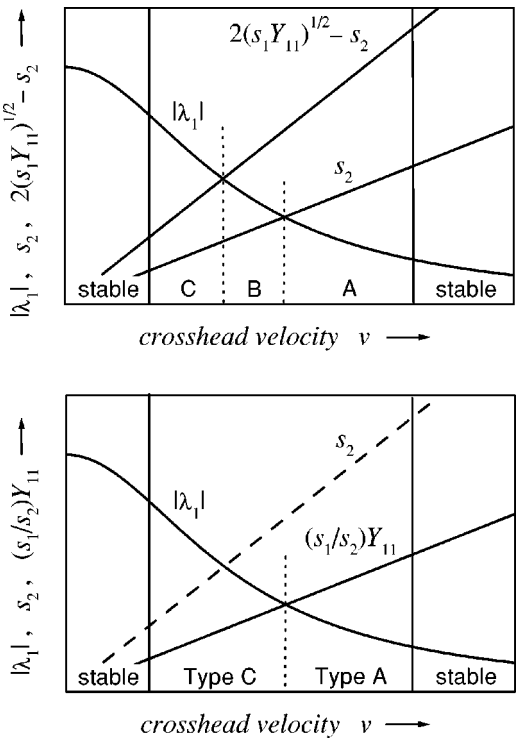

FIG. 21. Schematic illustration of the strain-rate ranges of the various PLC types (cf. the text). For $s_2<(s_1/s_2)Y_{11}$ an intermediate type-B range shows up (upper part) which is absent in the opposite case (lower part).

To summarize, when the PLC regime is scanned by increasing the crosshead velocity v, the following sequences of band types are possible in principle: s-C-B-A-s, s-B-A-s, s-C-B-s, s-C-A-s, s-A-s, s-C-s, and s-B-s where s stands for stable deformation behavior. As one infers from Fig. 8, the Cu-Al alloy of the present work exhibits a direct transition from type C to type A as the crosshead velocity is increased (s-C-A-s), whereas the intermediate type-B behavior (s-C-B-A-s) was observed, for instance, for an Al-Mg alloy by Balik and Lukac[26] as well as in our numerical simulations (Fig. 16; also see Ref. 71).

VII. CONCLUSIONS

The experimental investigations reported in this work have shown that laser extensometry provides a most valuable tool to analyze the spatiotemporal dynamics of plastic deformation bands associated with the PLC effect. A major advantage of this technique consists of the unambigous identification of the various types of deformation bands in terms of high-dimensional space-time correlation plots. This typification turned out to be not always possible in terms of scalar stress-strain curves alone. Moreover, laser extensometry al-

lows the precise determination of the band parameters: propagation velocity, band width and band strain.

Stimulated by the extensive data provided by laser extensometry and noting the lack of theoretical results on PLC deformation bands, a model of the PLC effect has been proposed in the present work. Our main concern was to account for DSA on a microphysical base, and not only in a phenomenological way, thus avoiding a shortcoming of previous models. Attention was also directed to the nature of the spatial coupling which governs the propagation of the deformation bands. It has been argued that long-range dislocation interactions lead to highly correlated dislocation glide which, in the PLC regime, becomes manifest on the macroscopic scale.

The salient feature of the model is the explicit incorporation of the DSA kinetics. The additional time scale associated with DSA plays an important role in the qualitative appearance of the PLC effect. For instance, at the onset of PLC instabilities, the DSA time scale determines the type of bifurcation (Hopf bifurcation). Moreover, DSA represents the reference time scale with respect to which the machine responds during discontinuous type-B band propagation. These features could not be explained appropriately in terms of previous models which implicitly assume the DSA kinetics to be in equilibrium with the dislocation dynamics [as in Penning's model (Refs. 28–33)] or which assume DSA to be close to dislocation dynamical equilibrium (as in McCormick's model,[17,39] where a linear relaxation is postulated for the DSA kinetics).

The differences between the present theory and the earlier approaches become particularly pronounced if mechanical tests at a constant *stress* rate are to be described ($\dot{\sigma}$ = const). Under this testing condition staircase-type stress-strain curves are observed with PLC bands propagating rapidly at virtually constant stress and quasielastic loading intervals separating the nucleation or propagation of successive bands. From a glance at the characteristic times involved (the duration of band propagation $t_{\mathrm{prop}} \approx 10^{-1}$ s is much less than the duration of the intermediate loading phases $t_{\mathrm{load}} \approx 10$ s) we conclude that most of the aging occurs during the elastic loading. In fact, as the characteristic time of solute diffusion $\eta^{-1} \approx 10 \ldots 100$ s largely exceeds t_{prop}, *dynamic* strain aging during band propagation is not significant at all, but *static* aging occurs during elastic loading. Obviously, this case cannot be described in terms of a DSA kinetics which is in, or close to, equilibrium with the dislocation dynamics. The present model, however, also covers the $\dot{\sigma}$ = const case, since it combines the interplay between static aging and dynamic depinning of dislocations. The extension of the theory and a quantitative interpretation of the experimental observations pertaining to $\dot{\sigma}$ = const tests will be presented in a forthcoming publication.

ACKNOWLEDGMENTS

Financial support of this work by a Heisenberg grant (P.H.) of the Deutsche Forschungsgemeinschaft and in the framework of the DFG Forschergruppe Ri339/15-3, as well as by the European TMR network FMRX-CT96-0062 on 'Instability in Deformation and Fracture' is gratefully acknowledged.

APPENDIX A: ESTIMATES OF SPATIAL COUPLING PARAMETERS

Deformation banding is associated with inhomogeneities in the plastic strain and strain rate which act back on the effective stress state in the deformation band. To leading order this effect can be expressed by diffusionlike coupling terms entering the balance of the DSA activation enthalpy g and/or of the mechanical driving f. From a qualitative point of view, various intrinsic propagation mechanisms can be imagined as follows.

(1) Obviously, the solute diffusion associated with DSA gives rise to a diffusive coupling in the dynamics of g. The corresponding diffusion coefficient, however, hardly exceeds $D \approx 10^{-6}$ mm^2/s. Hence this mechanism is too inefficient to establish the macroscopic spatial coupling observed with the PLC bands (on the mm scale with characteristic times in the s range).

(2) Similar arguments hold for the double cross-slip of screw dislocations (Refs. 49 and 61). While this mechanism also provides a random exchange of dislocations between parallel slip planes and, therefore, can be mapped on a diffusionlike coupling, cross-slip is unlikely to govern PLC band propagation from a quantitative point of view.

(3) As to polycrystalline materials investigated here, another spatial coupling is established by the compatibility stresses in the granular system.[61] Provided that intergranular stresses cannot be relaxed efficiently by plastic deformation, this mechanism may carry over to the macroscopic scale for coarse-grained materials. However, as no grain-size dependence of the band parameters was observed in the range $70 \ldots 530$ μm, we conclude that compatibility stresses do not prevail during band propagation.

Since the predominance of those coupling mechanisms seems unlikely in view of the experimental findings, we compare two other coupling mechanisms which are in accordance with the observation that the bandwidth w_b scales in proportion to the specimen thickness s: (i) bending moments according to Bridgman's analysis of a cylindrical neck, and (ii) a long-range correlated dislocation glide.

An *extrinsic* propagation mechanism proposed in Refs. 39 relates to the nonuniform, multiaxial stress state that develops around a PLC band. Due to the plastic strain gradients associated with deformation banding, deviations from the uniaxial tensile stress (bending moments associated with the Bridgman effect[51,39]) arise which scale with the square of the specimen thickness s. To see this, we note that, according to Bridgman, the actual stress in the presence of a cylindrical neck is $\sigma = \sigma_{\mathrm{ext}} F$,[51,39] where σ_{ext} represents the nominal applied stress and the correction factor

$$F = \left[\left(1 + \frac{2R}{r} \right) \ln \left(1 + \frac{r}{2R} \right) \right]^{-1} \approx 1 - \frac{r}{2R}. \qquad \text{(A1)}$$

Here r stands for the local specimen radius, and $R \gg r$ is the radius of curvature of the neck. With $R^{-1} \approx 2\partial_x^2 r$, and ex-

pressing the variation in r due to a spontaneously formed neck by the plastic strain variation $\Delta r/r_0 = -\Delta\epsilon/2$, the actual stress can be approximated by

$$\sigma \approx \sigma_{\rm ext}\left(1+\frac{r_0^2}{2}\partial_x^2\epsilon\right), \tag{A2}$$

where r_0 denotes the specimen radius outside the neck. While this holds for a cylindrically necked specimen, a similar stress correction is applicable to a deformation band in a flat specimen when the specimen radius r is replaced by the specimen thickness s,

$$\Delta\sigma = \sigma - \sigma_{\rm ext} = \beta_f s^2 \sigma_{\rm ext}\partial_x^2\epsilon, \tag{A3}$$

with a geometry factor $\beta_f \approx 0.25$.

As opposed to that extrinsic geometry effect, correlated dislocation glide affects, through long-range internal stress fields, the average effective stress $\sigma_{\rm eff} = \sigma_{\rm ext} - \sigma_{\rm int}$ acting on the mobile dislocations,

$$\Delta\sigma_{\rm eff} = \sigma_{\rm int}\frac{\rho_{\rm m}/2}{\rho_{\rm t}}\left[\frac{\epsilon_{,t}(x+\xi)-\epsilon_{,t}(x)}{\epsilon_{,t}(x+\xi/2)}+\frac{\epsilon_{,t}(x-\xi)-\epsilon_{,t}(x)}{\epsilon_{,t}(x-\xi/2)}\right]$$

$$\approx \sigma_{\rm int}\frac{\rho_{\rm m}}{2\rho_{\rm t}}\xi^2\partial_x^2(\ln\epsilon_{,t}), \tag{A4}$$

where $\rho_{\rm m}$ and $\rho_{\rm t}$ stand for the mobile and the total dislocation density, respectively, $\sigma_{\rm int}$ is the average internal stress (back stress) produced by dislocation interactions, and

$$\xi \approx \frac{\mu b}{4\pi\sqrt{\sigma_{\rm int}S_\infty}} \tag{A5}$$

denotes the correlation length (glide plane distance) over which dislocation interactions are strong enough as to induce correlated dislocation motion.[67–69] Equation (A4) reflects the idea that half of the mobile dislocations gliding on the planes $x \pm \xi = {\rm const}$ (those having the appropriate sign) support or obstruct dislocation glide on the reference plane $x = {\rm const}$, depending on whether they move faster or slower. The expression in square brackets then represents the relative frequency at which dislocations on $x = {\rm const}$ are overtaken by, or overtake, dislocations on $x \pm \xi = {\rm const}$. In the front and in the wake of the band where $S_\infty \to 0$, the correlation length diverges, such that correlations are only limited by the finite specimen thickness s. Assuming the band to be inclined at 45° with respect to the tensile axis, one has $\xi \to s/\sqrt{2}$.

According to the different physical mechanisms reflected by the stress correction [Eq. (A3)] owing to a gradient in plastic strain and by the strain-rate dependent correction [Eq. (A4)], the corresponding coupling mechanisms are formally distinct. To a first approximation, the Bridgman effect can be expressed as a diffusionlike coupling in f (i.e., $\partial_t f = D_f\partial_x^2 f + \cdots$), with the pseudodiffusion coefficient

$$D_f = \beta_f\frac{\sigma_{\rm ext}}{S_0}\epsilon_{,t}s^2. \tag{A6}$$

As opposed to this, dislocation correlations affect mainly the (nondimensional) depinning term in Eq. (11), $\dot g^{(-)} = -f\exp[-g]g = -[\epsilon_{,t}/(\eta\Omega)]g$ of the dynamics of g. As $\partial_x^2(\ln\epsilon_{,t}) \approx \partial_x^2 g$, this leads to $\dot g^{(-)} = \dot g_0^{(-)} - (D_g/\eta)\partial_x^2 g$ with

$$D_g = \frac{1}{4}\frac{\rho_{\rm m}}{\rho_{\rm t}}\frac{\sigma_{\rm int}}{S_0}\frac{\epsilon_{,t}}{\Omega}g\,s^2. \tag{A7}$$

Using the well-known relation between the internal stress and the total dislocation density, $\sigma_{\rm int} = \alpha\mu b\sqrt{\rho_{\rm t}}$, and expressing the elementary strain by $\Omega = b\rho_{\rm m}/\sqrt{\rho_{\rm t}}$ (shear modulus μ, length of the Burgers vector b, and numerical factor $\alpha \approx 0.4$), Eq. (A7) simplifies to $D_g \approx \beta_g g_{\rm min}(\mu/S_0)\epsilon_{b,t}s^2$ which is, up to a factor $(\beta_g g_{\rm min}/\beta_f)(\mu/\sigma_{\rm ext}) \approx 10^2$, of the form of Eq. (A6). From this we conclude that dislocation correlations provide the more efficient spatial coupling mechanism. Furthermore we note that, for simplicity, D_g is considered constant by replacing g and $\epsilon_{,t}$ by $g_{\rm min}$ and $\epsilon_{b,t}$, respectively, i.e. the values attained within a deformation band.

APPENDIX B: PERTURBATION ANALYSIS OF BAND TYPES B AND C

We perform the perturbation analysis in the comoving frame of a type-A band (velocity c). Here $[f_0(\tilde x), g_0(\tilde x)]$ is associated with the stationary profile of a type-A band which represents a steady-state solution of

$$\dot f = cf' + \dot\sigma f - \theta\exp[-g]f^2, \tag{B1}$$

$$\dot g = g'' + cg' + g_\infty - g - fg\exp[-g]. \tag{B2}$$

Let us now introduce deviations from solitary type-A behavior by writing $(g,f) = (g_0,f_0) + (\exp[-c\tilde x/2]y, u)$. (Extracting $\exp[-c\tilde x/2]$ from the perturbation in g makes the differential operator of y self-adjoint.) Linearization with respect to the small perturbations y and u gives, for the aging kinetics,

$$\dot y = y'' - \left(f_0\exp[-g_0](1-g_0)+1+\frac{c^2}{4}\right)y$$

$$-g_0\exp[-g_0]\exp[c\tilde x/2]u, \tag{B3}$$

while the mechanical perturbations obey the linear equation

$$\dot u = cu' + \dot\sigma_0 u + f_0\dot\sigma_1$$

$$-\theta f_0\exp[-g_0](2u - f_0\exp[-c\tilde x/2]y). \tag{B4}$$

Here the stress rate is split into the unperturbed contribution $\dot\sigma_0$ and the perturbation $\dot\sigma_1$ associated with deviations from type-A behavior: $\dot\sigma = \dot\sigma_0 + \dot\sigma_1$. According to the machine equation (8), the stress-rate perturbation reads

$$\dot\sigma_1 = s_1\int d\tilde x(f_0\exp[-g_0]\exp[-c\tilde x/2]y - \exp[-g_0]u)$$

$$\approx -\frac{s_2}{f_0}u + s_1\int d\tilde x f_0\exp[-g_0]\exp[-c\tilde x/2]y, \tag{B5}$$

with

$$s_1=\frac{\Omega E_{\rm eff}}{S_0 l}\sqrt{\frac{D_g}{\eta}},\quad s_2=\frac{E_{\rm eff}}{S_0}\frac{v}{\eta l}. \tag{B6}$$

For an investigation of types B and C bands, we may focus on the reaction of the tensile machine to plastic strain-rate fluctuations. This nonlocal mechanical feedback occurs on a fast time scale [Eq. (B5)]. For this reason, the following approximations can be applied to Eq. (B4).

(1) The stress rate $\dot{\sigma}_0$ in the absence of fluctuations is small and will be neglected.

(2) Variations associated with the *local* strain hardening (coefficient θ) are negligible as compared to the *nonlocal* machine response.

(3) For the same reason, gradients of u remain small, as the machine responds uniformly along the gauge length: $u'\approx 0$.

With these approximations Eq. (B4) reduces to

$$\dot{u}\approx f_0\dot{\sigma}_1\approx -s_2 u+s_1 f_0\int d\tilde{x} f_0\exp[-g_0]\exp[-c\tilde{x}/2]y. \tag{B7}$$

Equations (B3) and (B7) represent a system of linear integrodifferential equations the solution of which will tell us about the possibility of deformation bands of types B and C. To this end we integrate the mechanical response and write Eqs. (B3) and (B7) in formal analogy to a Schrödinger equation with additional inhomogeneity. This is achieved by setting

$$y=\exp[i\omega t]\psi,\quad u=\exp[i\omega t]\varphi \tag{B8}$$

with a complex-valued frequency $\omega=\Re(\omega)+i\Im(\omega)$. This ansatz gives

$$i\omega\psi+\mathcal{H}\psi=-\mathcal{Y}, \tag{B9}$$

with the "Hamiltonian" $\mathcal{H}=-\partial_{\tilde{x}}^2+\mathcal{V}$, the "potential"

$$\mathcal{V}=f_0\exp[-g_0](1-g_0)+1+\frac{c^2}{4}, \tag{B10}$$

and the ψ dependent "inhomogeneity"

$$\mathcal{Y}=\frac{s_1}{s_2+i\omega}f_0 g_0\exp[-g_0]\exp[c\tilde{x}/2]\times\int d\tilde{x}' f_0\exp[-g_0]\exp[-c\tilde{x}'/2]\psi. \tag{B11}$$

Note that ψ describes the perturbed aging kinetics, while the mechanical response enters through the inhomogeneity $\mathcal{Y}$.

The formal solution of (B9)–(B11) is obtained by an expansion of ψ and $\mathcal{Y}$ in terms of the Hamiltonian's eigenfunctions ϕ_n pertaining to eigenvalues λ_n, namely, $\mathcal{H}\phi_n=\lambda_n\phi_n$,

$$\psi=\sum_{n=1}^{\infty}c_n\phi_n,\quad \mathcal{Y}=\sum_{n=1}^{\infty}d_n\phi_n, \tag{B12}$$

with coefficients c_n and d_n, respectively. Then Eq. (B9) reads

$$\sum_{n=1}^{\infty}[(i\omega+\lambda_n)c_n+d_n]\phi_n=0. \tag{B13}$$

Making use of orthonormality of the eigenfunctions, $\int d\tilde{x}\phi_n\phi_m^*=\delta_{nm}$, we obtain

$$d_n=-(i\omega+\lambda_n)c_n=\int d\tilde{x}\phi_n^*\mathcal{Y}=\frac{s_1}{s_2+i\omega}\sum_{m=1}^{\infty}c_m Y_{nm}, \tag{B14}$$

with the coefficient matrix

$$Y_{nm}=\int d\tilde{x}\phi_n^* f_0 g_0\exp[-g_0]\exp[c\tilde{x}/2]\times\int d\tilde{x}'\phi_m f_0\exp[-g_0]\exp[-c\tilde{x}'/2]. \tag{B15}$$

The solvability condition of the algebraic problem [Eq. (B14)] reads

$$\det\left[\frac{s_1}{s_2+i\omega}Y_{nm}+(i\omega+\lambda_n)\delta_{nm}\right]=0. \tag{B16}$$

The determination of the set of eigenfunctions $\{\phi_n\}$ and of the corresponding spectrum $\{\lambda_n\}$ is complicated by the fact that the explicit $\tilde{x}$ dependence of potential (B10) is not exactly known. However, from definition (B10) and the qualitative behavior of the unperturbed type-A solution, we know that $\mathcal{V}$ represents a double-well potential, as depicted in Fig. 20. Corresponding to the minima of $\mathcal{V}$, perturbations tend to be localized preferentially in the band front where dislocations are depinned from their solute clouds, and in the wake of the band where dislocations are recaptured. Furthermore, we know that the ground state of $\mathcal{H}$ represents the only bounded state of $\mathcal{V}$ ($\lambda_1<0$, $\lambda_n\geqslant 0$ for $n\geqslant 2$). This is clear from the fact that the Goldstone mode, while having a zero eigenvalue $\lambda_2=0$, possesses one node: $\phi_2\propto\exp[c\tilde{x}/2]g_0'$. (This zero mode restores the translational invariance which is broken by the presence of the type-A band $[g_0(\tilde{x}),f_0(\tilde{x})]$.) As the eigenvalues of a Sturm-Liouville problem increase with increasing number of zeros of the corresponding eigenfunctions, the node-free ground state (index $n=1$) must possess a negative eigenvalue. This state is governing the stability of the type-A band with respect to perturbations of types B and C.

For a qualitative discussion of the way a type-A band loses stability, we restrict ourselves to the perturbations induced by that ground-state eigenfunction ϕ_1. This represents a bimodal function with extrema in the front and in the wake with respect to the unperturbed type-A band. If the ground mode is oscillating $[\Re(\omega)\neq 0]$, the superposition with the type-A solution represents a breather mode in the comoving frame. Transferred to the laboratory frame, this breather is associated with type-B behavior, i.e., intermittent band propagation with the concomitant serrations in the stress-

strain curve. If, however, the ground mode is growing without oscillations [$\Re(\omega)=0$, $\Im(\omega)<0$] the resulting solution is either blowing up while it is slowing down or it is fading away, depending on the sign of the ground mode. In both cases, type-C behavior results as the propagation of the band tends to be suppressed.

To obtain a more quantitative idea, we assume that the elements of the coefficient matrix $Y_{1m}\approx 0$ for $m>1$, such that Eq. (B16) is solved by

$$\frac{s_1}{s_2+i\omega}Y_{11}+i\omega-|\lambda_1|\approx 0. \tag{B17}$$

After separation of real and imaginary parts, one obtains Eqs. (38) and (39), which are discussed in Sec. VI.

*Electronic address: hahner@jrc.nl

[1] A.H. Cottrell and B.A. Bilby, Proc. R. Soc. London, Ser. A **62**, 49 (1949); A.H. Cottrell, Philos. Mag. **44**, 829 (1953).
[2] A.W. Sleeswyk, Acta Metall. **6**, 598 (1958).
[3] D. Munz and E. Macherauch, Z. Metallkd. **57**, 552 (1966).
[4] W. Räuchle, O. Vöhringer, and E. Macherauch, Z. Metallkd. **64**, 296 (1973); Mater. Sci. Eng. **12**, 147 (1973).
[5] B.J. Brindley and P.J. Worthington, Metall. Rev. **15**, 101 (1970).
[6] A. Wijler, J. Schade van Westrum, and A. van den Beukel, Acta Metall. **20**, 355 (1972).
[7] L.J. Cuddy and W.C. Leslie, Acta Metall. **20**, 1157 (1972).
[8] G. Guillot and J. Grilhe, Acta Metall. **20**, 291 (1972).
[9] P.G. McCormick, Acta Metall. **19**, 463 (1971); **20**, 352 (1972); **21**, 873 (1973).
[10] S.H. van den Brink, A. van den Beukel, and P.G. McCormick, Phys. Status Solidi A **30**, 469 (1975).
[11] A. van den Beukel, Phys. Status Solidi A **30**, 197 (1975).
[12] R.A. Mulford and U.F. Kocks, Acta Metall. **27**, 1125 (1979).
[13] N. Louat, Scr. Metall. **15**, 1167 (1981).
[14] E. Pink and A. Grinberg, Mater. Sci. Eng. **51**, 1 (1981); Acta Metall. **30**, 2153 (1982).
[15] A. van den Beukel and U.F. Kocks, Acta Metall. **30**, 1027 (1982).
[16] R.B. Schwarz and L.L. Funk, Acta Metall. **31**, 299 (1983); **33**, 295 (1985).
[17] P.G. McCormick, Trans. Indian Inst. Met **39**, 98 (1986).
[18] K. Chihab, Y. Estrin, L.P. Kubin, and J. Vergnol, Scr. Metall. **21**, 203 (1987).
[19] E. Pink, Acta Metall. **37**, 1773 (1989).
[20] C.P. Ling and P.G. McCormick, Acta Metall. Mater. **41**, 3127 (1993).
[21] A. Kalk and Ch. Schwink, Phys. Status Solidi B **172**, 133 (1992); Philos. Mag. A **72**, 315 (1995).
[22] A. Kalk, A. Nortmann, and Ch. Schwink, Philos. Mag. A **72**, 1239 (1995).
[23] A. Nortmann and Ch. Schwink, Acta Metall. **45**, 2043 (1997); **45**, 2051 (1997).
[24] F. Springer and Ch. Schwink, Scr. Metall. Mater. **25**, 2739 (1991); **32**, 1771 (1995).
[25] F. Springer, A. Nortmann, and Ch. Schwink, Phys. Status Solidi A **170**, 63 (1998).
[26] J. Balik and P. Lukac, Acta Metall. **41**, 447 (1993).
[27] M.A. Lebyodkin and L.R. Dunin-Barkovskii, Phys. Solid State **40**, 447 (1998).
[28] P. Penning, Acta Metall. **20**, 1169 (1972).
[29] Y. Estrin and L.P. Kubin, Acta Metall. **28**, 965 (1980); Res. Mech. **23**, 197 (1988).
[30] L.P. Kubin and Y. Estrin, Acta Metall. **33**, 397 (1985).
[31] H.M. Zbib and E.C. Aifantis, Res. Mech. **23**, 261 (1988); Scr. Metall. **22**, 1331 (1988).
[32] L.P. Kubin and Y. Estrin, Acta Metall. Mater. **38**, 697 (1990); Phys. Status Solidi B **172**, 173 (1992).
[33] P. Hähner, Mater. Sci. Eng., A **164**, 23 (1993).
[34] Y. Estrin, L.P. Kubin, and E.C. Aifantis, Scr. Metall. Mater. **29**, 1147 (1993).
[35] M.A. Lebyodkin, Y. Brechet, Y. Estrin, and L.P. Kubin, Phys. Rev. Lett. **74**, 4758 (1995).
[36] G. Ananthakrishna, S.J. Noronha, C. Fressengeas, and L.P. Kubin, Phys. Rev. E **60**, 5455 (1999).
[37] F. Mertens, Scott V. Franklin, and M. Marder, Phys. Rev. Lett. **78**, 4502 (1997).
[38] Scott V. Franklin, F. Mertens, and M. Marder, Phys. Rev. E **62**, 8195 (2000).
[39] P.G. McCormick and C.P. Ling, Acta Metall. Mater. **43**, 1969 (1995).
[40] P. Hähner, Mater. Sci. Eng., A **207**, 208 (1996); **207**, 216 (1996).
[41] M. Zaiser and P. Hähner, Phys. Status Solidi B **199**, 267 (1997).
[42] P. Hähner, Acta Mater. **45**, 3695 (1997).
[43] A. Korbel, Scr. Metall. **8**, 609 (1974); A. Korbel and H. Dybiec, Acta Metall. **29**, 89 (1981).
[44] W. Bochniak, Z. Metallkd. **90**, 153 (1999).
[45] A. Nortmann and H. Neuhäuser, Mater. Sci. Eng., A **234-236**, 548 (1997); Phys. Status Solidi A **168**, 87 (1998).
[46] H. Neuhäuser, J. Plessing, and W. Schülke, J. Mech. Beh. Met. **2**, 231 (1990).
[47] C. Engelke, J. Plessing, and H. Neuhäuser, Mater. Sci. Eng. **164**, 235 (1993).
[48] L.B. Zuev and V.I. Danilov, Philos. Mag. A **79**, 43 (1999).
[49] V. Jeanclaude and C. Fressengeas, Scr. Metall. Mater. **29**, 1177 (1993).
[50] P. Hähner, Appl. Phys. A: Solids Surf. **58**, 41 (1994).
[51] P. W. Bridgman, *Studies in Large Plastic Flow and Fracture* (McGraw-Hill, New York, 1952).
[52] Y. Estrin and L. Kubin, *Continuum Models for Materials with Microstructure* (Wiley, New York, 1995), Chap. 12.
[53] A. Wijler and J. van Westrum, Scr. Metall. **5**, 531 (1971).
[54] S. Miura, A. Haerian, and S. Hashimoto, J. Mater. Sci. **22**, 3446 (1987).
[55] R.W. Balluffi and A.V. Granato, in *Dislocations in Solids* 4, edited by F.R.N. Nabarro (North-Holland, Amsterdam, 1979).
[56] J. Schade van Westrum and A. Wijler, Acta Metall. **21**, 1079 (1973).
[57] P.G. McCormick, S. Venkadesan, and C.P. Ling, Scr. Metall. Mater. **29**, 1159 (1993).
[58] A. Ziegenbein, Ph.D thesis, TU Braunschweig, 2000.
[59] P.G. McCormick, Philos. Mag. **20**, 949 (1970).
[60] W. Charnock, Philos. Mag. **18**, 89 (1968).
[61] P. Hähner, Scr. Metall. Mater. **29**, 1171 (1993).
[62] F.R. Brotzen and A. Seeger, Acta Metall. **37**, 2985 (1989).
[63] J. Schlipf, Scr. Metall. Mater. **31**, 909 (1994).

[64] P. Sapalidis, D. Dodou, P. Hähner, M. Zaiser, and E.C. Aifantis, in *Influences of Interface and Dislocation Behavior on Microstructure Evolution*, edited by M. Aindow, M. Asta, M.V. Glazov, D.L. Medlin, A.D. Rollet, and M. Zaiser, MRS Symposia Proceedings No. 652 (Materials Research Society, Pittsburgh, 2001), p. Y8.26.
[65] P. Hähner and Y. Drossinos, Phys. Rev. E **59**, R6231 (1999).
[66] E.C. Aifantis, Int. J. Plast. **3**, 211 (1987); Int. J. Eng. Sci. **30**, 1279 (1992).
[67] P. Hähner, Appl. Phys. A: Mater. Sci. Process. **62**, 473 (1996); Acta Mater. **44**, 2345 (1996).
[68] P. Hähner and M. Zaiser, Phys. Rev. Lett. **81**, 2470 (1998).
[69] M. Zaiser and E.C. Aifantis, Appl. Phys. A: Mater. Sci. Process. **66**, 393 (1998).
[70] F. Chmelik, J. Dosoudil, J. Plessing, H. Neuhäuser, P. Lukac, and Z. Trojanova, Key Eng. Mater. **97-98**, 263 (1994).
[71] E. Rizzi and P. Hähner (unpublished).